

# Scaling of Steady States in a Simple Driven Three-State Lattice Gas

Michael Thies

Thesis submitted to the Faculty of the  
Virginia Polytechnic Institute and State University  
in partial fulfillment of the requirements for the degree of

Master of Science  
in  
Physics

Beate Schmittmann, Chair  
Royce K.P. Zia  
James R. Heflin

September 9, 1998  
Blacksburg, Virginia

Keywords: Driven Lattice Gas, Scaling, Monte Carlo Simulation, Mean-Field  
Theory

Copyright 1998, Michael Thies

# Scaling of Steady States in a Simple Driven Three-State Lattice Gas

Michael Thies

(ABSTRACT)

Phase segregated states in a simple three-state stochastic lattice gas are investigated. A two dimensional finite lattice with periodic boundary conditions is filled with one hole and two oppositely “charged” species of particles, subject to an excluded volume constraint. Starting from a completely disordered initial configuration, a sufficiently large external “electric” field  $E$  induces the phase segregation, by separating the charges into two strips and “trapping” the hole at an interface between them. Focusing on the steady state, the scaling properties of an appropriate order parameter, depending on drive and system size, are investigated by mean-field theory and Monte Carlo methods. Density profiles of the two interfaces in the ordered system are studied with the help of Monte Carlo simulations and are found to scale in the field-dependent variable  $\mathcal{E} = 2 \tanh(E/2)$ , for  $E \lesssim 0.8$ . For larger values of  $E$ , independent approximations of the interfacial profiles, obtained within the framework of mean-field theory, exhibit significant deviations from the Monte Carlo data. Interestingly, the deviations can be reduced significantly by a slight modification of the mean-field theory.

# Contents

<b>1</b>	<b>Introduction</b>	<b>1</b>
1.1	Background and Motivation . . . . .	1
1.2	Overview . . . . .	3
<b>2</b>	<b>The Model System</b>	<b>5</b>
2.1	The Microscopic Model . . . . .	5
2.2	Control and Order Parameters . . . . .	7
2.3	The Phase Transition . . . . .	8
2.4	Technical Details of the Simulations . . . . .	9
2.5	Mean Field Equations . . . . .	10
<b>3</b>	<b>Steady-State Results</b>	<b>15</b>
3.1	Monte Carlo Simulations . . . . .	15
3.2	Scaling of the Order Parameter . . . . .	18
3.3	Scaling of the Charge and Hole Density . . . . .	22
3.4	Size and Field Dependence of Charge and Hole Density . . . . .	24

3.4.1	Simulations with varying $L_y$ . . . . .	24
3.4.2	Simulations with different $E$ . . . . .	26
3.5	Independent Interface Approximation . . . . .	29
<b>4</b>	<b>Conclusions</b>	<b>42</b>
4.1	Summary . . . . .	42
4.2	Further Discussion . . . . .	44
4.3	Outlook . . . . .	46
	<b>Bibliography</b>	<b>48</b>
<b>A</b>	<b>Source Codes</b>	<b>51</b>
A.1	Typical C Source Code for the Simulations . . . . .	51
A.2	An Alternative Algorithm . . . . .	60
	<b>Vita</b>	<b>62</b>

# Chapter 1

## Introduction

### 1.1 Background and Motivation

Physical systems in non-equilibrium states have attracted considerable interest in the past decade [1]. If compared to equilibrium systems, a wealth of unexpected phenomena is present. However, they are mostly poorly understood. So, it is natural to investigate first the simplest systems among non-equilibrium ones even if they are not easily realized experimentally due to the simplification. For this reason, many investigations have focused on driven stochastic lattice gases which constitute one of the simplest non-equilibrium generalizations of the well known equilibrium Ising model. Interesting properties, which are found in these driven lattice gases, include new universality classes for critical behavior [4], [5], long-range correlations even far from the critical temperature [6], and anomalous low-temperature properties [7]. In the “standard” model, introduced in 1983 by Katz et. al. [2], particles in an Ising lattice gas with periodic boundary conditions hop stochastically to empty nearest-neighbor sites, governed by the energetics of the Ising Hamiltonian, coupled to a heat bath and a driving field which favors (suppresses) jumps along (against) a particular lattice direction. Monte Carlo simulations have shown that the system undergoes a continuous phase transition from a disordered to a phase-segregated steady state at a field-dependent temperature. Using field theoretic and renormalization group techniques [3], critical properties could be computed [4] which were later confirmed by computer simulations [8]. A review can be found in [1].

Many variations of this standard model have been investigated in order to get a deeper understanding of this class of non-equilibrium systems (for a review, see

again [1], especially Chapter 6). In this work, we focus on one particular generalization of the standard model. Inspired by natural extensions of equilibrium Ising systems such as the Potts [13], Ashkin–Teller [14], Blume–Emery–Griffiths [15] or ANNNI [16] models in which the on-site variable can take more than two values, we investigate a lattice gas with two species of particles (referred to as positive and negative “charges”) and holes, driven by an external field. In addition to our primary theoretical interests, these studies are also motivated by real physical systems, where more than one species of particles may be present. Examples are certain fast ionic conductors where two different ion species act as charge carriers [9] or water-in-oil microemulsions where small water droplets suspended in oil carry electric charge ( $\pm e$ ) [10]. In both systems, small changes of electric field or charge carrier density may cause drastic changes of the conductivity. Other examples of three-state systems include traffic flow models [11] and the Duke–Rubinstein model [12] for gel electrophoresis, which is a technique to separate charged polymers by molecular weight.

In our model, the three-state lattice gas consists of holes and two distinct species of particles driven by an external field in opposite directions. This external field breaks the (Potts) symmetry of the stochastic variable by suppressing the hopping of particles against the field. Furthermore, the only interaction between the particles is an excluded volume constraint so that only particle–hole exchanges can take place. In the absence of interparticle interactions, the temperature dependence of the system, reflecting a coupling to a heat bath, may be absorbed into the electric field. Hence, the model is a high–field, high–temperature approximation of a more complicated, interacting system.

This model was first introduced 1992 by Schmittmann et. al. [17]. Using a fully periodic square lattice containing an equal number of positive and negative “charges”, these authors discovered that the system undergoes a blocking phase transition controlled by field strength and particle density, separating a homogeneous phase from a spatially inhomogeneous one. For small mass densities and small external fields, the steady–state configurations are found to be disordered, so that both particle densities are homogeneous and a substantial charge current persists. In contrast, if a threshold mass density is exceeded, the particles form a single compact strip transverse to the field while the rest of the lattice remains essentially empty. The particle-rich region itself consists of two strips, also oriented transverse to the field, each dominated by one single species. In this phase, the particles impede one another, due to the excluded volume constraint, so that the charge current is much smaller. The model is discussed further in ref. [18], where a topologically distinct ordered phase (barber poles) was found and analyzed. An

analytical solution in the frame of a mean field theory was presented in ref. [20]. This work is continued here. With a slight geometrical modification, the model was also investigated by Foster and Godrèche [19].

Beyond continuing these earlier studies, our work is related to another important problem. In many scientific and technical areas, the dynamics of ordering in bulk systems, following a rapid temperature quench [22], is of major relevance. Defects or vacancies may control the disordering [23] or ordering process, especially if their dynamics is fast compared to that of the bulk system. This is the case in the present model. Recalling the excluded volume constraint, the dynamics of the defect is clearly faster than that of the bulk system, which is actually static except around the hole. Before investigating ordering processes, a good understanding of the final steady states is clearly crucial.

Here, we investigate the model introduced in [17] with only one vacancy (hole, defect). Thus, the lattice is completely filled with particles, except a single site which is occupied by the vacancy. The particle numbers of each species differ by at most one particle. Starting from a disordered initial configuration, the particles can only hop to the vacant site but may not exchange among themselves. As a result, the hole wanders through the lattice. Since the external field biases the hopping, the two particle species eventually segregate near the hole, moving in opposite directions. The hole itself ends up “trapped”, for large periods of time, on one of the two interfaces between the two ordered, particle-rich regions. These ordered regions can only grow when the hole “escapes”. When the steady state is finally reached, the lattice is filled by two strips, filled predominantly by positive and negative particles, respectively. The location of the single vacancy is the “remnant” of the empty region (strip) mentioned in the previous paragraph. We should stress, however, that the ordering process only takes place if the external field exceeds a certain system-size (i.e., mass) dependent threshold, corresponding to the transition line of [17]. The discussion of the steady state and its associated scaling properties is the subject of the following studies.

## 1.2 Overview

In the first Section of Chapter 2, we give a precise definition of the microscopic model, including the details of the Monte Carlo simulations such as the transition probabilities and time scales. The control and order parameters of the system are listed in Sec. 2.2, followed by a description of the two phases (Sec. 2.3). Technical

details of the simulations are outlined in Sec. 2.4. Finally, in the last section of this chapter, Sec. 2.5, we show how the mean field equations of the model system can be derived and summarize briefly their solution.

The third and main chapter begins with a discussion of the ordering process and the self-trapping mechanism of the hole, illustrated by snapshots of the system (Sec. 3.1). In the following, we focus on the steady states of the system. First, an order parameter [17] is calculated within mean field theory (Sec. 3.2). The result is then compared with Monte Carlo simulations. In Sec. 3.3, the scaling of the hole and particle densities, in terms of an appropriate scaling variable proposed in Sec. 2.5, is tested by computer simulations. More detailed data for these densities are reported in Sec. 3.4, where field strength and system size are varied independently. In Sec. 3.5, the profiles of the two steady-state interfaces characterizing the ordered phase are evaluated approximately, treating each interface independently from the other. There, a careful comparison with Monte Carlo data reveals systematic deviations for large fields. An improvement of the analytic forms is given on a heuristic level.

Chapter 4 concludes the thesis with a summary and some general remarks. The source code of the simulation program, written in C, is listed in the Appendix.

# Chapter 2

## The Model System

### 2.1 The Microscopic Model

Our model consists of a two-dimensional square lattice of  $L_x \times L_y$  sites with fully periodic boundary conditions. Each site can be either occupied by a positive or negative particle except a single site of the lattice, which remains empty. We should emphasize, that even though we refer to the particles as “charged”, they do not interact via the usual Coulomb potential. Instead, they interact only via the excluded volume constraint. An occupation variable  $n_{xy}^+$  ( $n_{xy}^-$ ) can be introduced, taking the value  $+1$  ( $-1$ ) if a positive (negative) charge is present at the site with the coordinates  $x, y$  and zero otherwise. In the absence of the external field, the two species are indistinguishable, so that the hole (empty site) would exchange randomly with a nearest-neighbor particle, independent of its charge and the direction of its move. This symmetry is broken by the electric field  $E$ , which is chosen to be uniform in space and time and is directed along the positive  $y$ -axis (longitudinal direction). In the presence of  $E$ , positively and negatively charged particles are driven into opposite directions. Here again, one should be cautious: the drive mimics an “electric” field only in how it couples to the charges of the particles.

A few more details must be provided to describe the simulations. All runs start from random configurations. In each Monte Carlo step (MCS), one of the four nearest-neighbor particles of the hole is chosen randomly. The transition probability for its exchange with the hole is given by the Metropolis rates [24]:

$$W = \frac{1}{\tau_s} \cdot \min \{1, e^{q \cdot \delta y \cdot E}\}, \quad (2.1)$$

where  $q = \pm 1$  is the charge of the particle,  $\delta y = 0, \pm 1$  is the change of the  $y$ -coordinate of the particle due to the jump, and  $\tau_s = 1$  is an (arbitrary) time scale. This choice mimics the local energetics of exchanges in a uniform field. Thus, a random number  $r$  is drawn between 0 and 1 and the exchange is performed only if  $r < W$ . Time is measured in units of Monte Carlo steps (MCS) and is incremented by one after each event (trial).

The dynamic interpretation of the model is based on the associated master equation [25]. If  $P(C, t)$  is the probability to find the system in the configuration  $C = \{n_{xy}^+, n_{xy}^-\}$  at the time  $t$ , the time evolution is governed by

$$\frac{\partial}{\partial t} P(C, t) = \sum_{C'} \{W(C' \rightarrow C)P(C', t) - W(C \rightarrow C')P(C, t)\}. \quad (2.2)$$

In this master equation,  $W(C \rightarrow C')$  is the transition rate from  $C$  to  $C'$ , which is specified by the Metropolis rates (2.1). In this context, the factor  $\tau_s$  from Eq. (2.1) determines the number of MCS performed per unit time. The positive contribution to the sum describes the rate for all processes which arrive in configuration  $C$ , while the negative term sums the rate of all processes where  $C$  loses to another configuration. Clearly, the former term increases while the latter decreases, the probability of the considered configuration. Under fairly general conditions,  $P(C, t)$  approaches a unique steady-state solution  $P^*(C)$  in the limit  $t \rightarrow \infty$  such that the two sums cancel exactly. However, the explicit form of  $P^*(C)$  is not easily found. Due to the periodic boundary conditions, there is no uniquely defined static potential here so that  $P^*(C)$  is not the familiar Boltzmann factor. The transition rates are chosen to satisfy detailed balance only with respect to a *local* potential, leaving the general detailed balance condition [25]

$$W(C' \rightarrow C)P^*(C') = W(C \rightarrow C')P^*(C). \quad (2.3)$$

unfulfilled.

Although it is not possible to derive a solution of the linear master equation, Eq. (2.2), for arbitrary  $E$ , the trivial solution for  $E = 0$  can be read off immediately. In this case, the system is in equilibrium: the particles diffuse randomly and  $P^*(C)$  is independent of the configuration ( $P^* \propto 1$ ).

## 2.2 Control and Order Parameters

The particle number of each species is conserved separately. As a consequence, the total particle number (mass) and the net charge are also conserved. With the help of the occupation variables, the overall mass density can be defined:

$$m = \frac{1}{L_x L_y} \sum_{x,y} (n_{xy}^+ + n_{xy}^-) \quad (2.4)$$

In our model system, containing only one hole, the mass density is given explicitly by  $m = 1 - 1/(L_x L_y)$  and therefore depends on the system size. However, the correction  $1/(L_x L_y)$  is less than 0.3%, even for the smallest lattice ( $16 \times 16$ ) considered here, so that  $m = 1$  is an excellent approximation which will be made in all of the following discussions. The statistical error of the simulation results is of the order of 5% (standard deviation of 100 runs in the steady state) and thus much larger.

The net charge depends on system size. It is zero for an odd number of total sites and  $-1$  for an even number (the hole always takes the place of a positive particle). In the simulations, this small difference does not appear to lead to observable effects. (This is, of course, not the case for net charge of  $O(L_x \times L_y)$ , see [26]). Therefore, the net charge is set equal to zero in further discussions.

A further control parameter is the electric field  $E$  which controls the biased motion of the particles, specified by the Metropolis rates (2.1). And for completeness, we have to mention  $L_x$  and  $L_y$  as the parameters which set the system size.

For later reference, the local hole and charge densities are introduced here:

$$\phi_{xy} = 1 - (n_{xy}^+ + n_{xy}^-) \quad \text{and} \quad \psi_{xy} = n_{xy}^+ - n_{xy}^- \quad (2.5)$$

Noting that the system does not exhibit inhomogeneities in the  $x$ -direction (for the investigated aspect ratios [18]), it is natural to focus on profiles averaged over the  $x$ -axis. The *profiles* of the hole and charge densities are defined via

$$\phi(y) = \frac{1}{L_x} \sum_x \phi_{xy} \quad \text{and} \quad \psi(y) = \frac{1}{L_x} \sum_x \psi_{xy} \quad (2.6)$$

For the quantitative analysis of the phase transition, we define the order parameter

$$Q_L = \frac{1}{m L_y} \left\langle \sum_y (\psi(y))^2 \right\rangle \quad (2.7)$$

following Ref. [17]. The angular bracket denotes the average over a simulation run.  $Q_L$  allows us to distinguish ordered from disordered configurations: Since the square prevents cancellations due to summing or averaging,  $Q_L$  is  $O(1)$  in the ordered phase, while being of order  $1/(mL_x)$  [17] in the disordered phase. Roughly speaking,  $mL_y Q_L$  counts the ordered rows transverse to the external field.

Since not only plots of order parameters but also of charge and hole density profiles are presented in the following, a remark on their averaging procedure is also necessary. While averaging  $Q_L$  over a given run is rather simple, by first measuring  $Q_L$  for each sample and then averaging these data, some effort is needed to derive the averaged density profiles from the configurational data. Due to translation invariance, strips can be centered at arbitrary  $y$ . Thus, just averaging  $\psi(y)$ , for fixed  $y$ , leads to unwanted cancellations which “wash out” any inhomogeneities. Thus, we always have to shift the ordered strips in such a way that their centers of mass coincide before we average. A natural choice would be to center all strips on, e.g.  $y = 0$ , by normalizing the phase of the largest wavelength Fourier component of the profile [27], [28]. This is particularly useful when profiles are measured near the phase transition. Here, however, we will mostly take data deeply in the ordered phase, where the hole is essentially “trapped” between the ordered regions. Thus, for each run, we keep track of the  $y$ -position of the hole and determine the maximum of the hole density after a large number of MCS. This maximum marks the interface between the positively and negatively dominated regions, the former located “up-field” from the latter, and the charge density profiles from different runs can now be shifted accordingly and averaged. Clearly, this procedure would run into difficulties if the interface were to wander significantly while the data for the hole density profile are being accumulated. However, for the choices of the control parameters considered here, this does not appear to present major problems since fluctuations of the interface location are rather small. Moreover, they are very slow; thus, the time scales over which the interface remains well localized are sufficiently large to determine the maximum of the hole density quite precisely.

## 2.3 The Phase Transition

Even though the blocking transition is not the major focus of this work, we provide some background here, following earlier discussions for arbitrary mass densities [17], [18] and [1].

Two distinct phases are observed in the system. For low values of drive and total

mass, the system is in the disordered phase, characterized by spatially uniform mass and charge densities. A significant amount of charge current flows in this phase. As  $E$  or  $m$  increase, a transition into an ordered phase, with spatially inhomogeneous densities, occurs. For systems with aspect ratios near unity, each species of particles forms a compact, stable strip transverse to the electric field. The strip of positive charges is located directly “upfield” from the negative strip, so that the strips block each other, due to the excluded volume constraint. The rest of the lattice remains essentially empty. Clearly, the current is much smaller in this phase. Here, we will investigate the structure of these transverse strips, when the empty region has shrunk to a single hole.

For completeness, we note that, for large aspect ratios  $L_x/L_y$ , tilted strips are observed in addition to transverse ones. These “barber poles” have nonzero winding number around the fully periodic lattice [18], [1]. For the aspect ratios considered here, they do not occur.

We conclude with some comments about the transition line. The simulations indicate that the threshold mass,  $m_c$ , depends strongly on  $E$  and the longitudinal system length  $L_y$ , but only weakly (if at all) on  $L_x$ . In our problem, where only a single hole is present, the mass density is fixed at unity, to excellent accuracy. Therefore, the transition is controlled by  $E$  and  $L_y$ . An explicit expression, within the framework of mean-field theory, will be provided in Sec. 2.5.

## 2.4 Technical Details of the Simulations

In the simulations presented in [17], nearest-neighbor pairs are chosen at random and then updated according to the transition rates (2.1), provided the pair consists of one particle and one hole. After  $L_x \times L_y$  trials, the number of MCS is incremented by 1. Clearly, such a procedure would be highly inefficient in our case, since the lattice is nearly filled. Instead, we attempt to update only nearest-neighbors of the hole, and count each trial as a MCS. Thus, the time scale here is the same as in Ref. [17].

This algorithm is not optimal since some exchange attempts are still unsuccessful. It is possible to speed up the simulations further, by updating every trial and incrementing the MC time by an appropriate factor, determined by the transition probabilities and the local neighborhood of the move (see Appendix, Sec. A.2 and also [25]). However, we use the slower algorithm here, since it simplifies the averag-

ing over different runs.

In our simulations,  $E$  varies between 0.2 and 2.0. The system sizes  $L_x$  and  $L_y$  range from 16 to 48 lattice sites. Since configurations are typically homogeneous in the  $x$ -direction,  $L_x$  is restricted to 16 sites unless we specifically wish to explore the  $L_x$  dependence of key quantities. For all systems, the initial configuration is random. The random number generator (see the program printout in A.1) is taken from Numerical Recipes [29].

The UNIX-machine used for the simulations is a dec- $\alpha$  machine, which performed about  $5.4 \times 10^8$  MCS per hour using the Metropolis algorithm. A system with  $16 \times 24$  sites at  $E = 0.8$  (as discussed at the beginning of Sec. 3.1) requires approximately  $5 \times 10^7$  MCS to reach the steady state. In addition, 100 runs are needed in order to have a statistically reliable average of  $Q_L$ . The associated real time of this simulation is then  $10h$ . However, with growing system size  $L_y$  or electric field  $E$ , considerably more MCS are needed to reach the steady state, due to the slow ordering dynamics of the system. To be specific, one of our longest runs lasted  $4 \times 10^8$  MCS for a system of size  $16 \times 36$  at field  $E = 0.8$ . By performing 100 runs in order to get an average, the simulation takes over  $55h$ . Thus, the real time requirements set the limit for our simulation studies.

## 2.5 Mean Field Equations

Even though the master equation is just a linear equation, in practice it is not susceptible to theoretical analysis. To proceed, a continuum model was introduced in the form of equations of motion for the conserved quantities [17]. These can be derived using a phenomenological approach [17] or directly from the master equation [28]. Here, we summarize the latter approach, in order to get a quantitative understanding of the effective drive appearing in the continuum equations. First, we consider the one-dimensional problem, retaining only the field direction, for simplicity. Thus, particle moves are biased according to the Metropolis rates (2.1). We introduce the occupation variable  $p_i$  ( $n_i$ ), being one or zero, depending on whether a positive (negative) charge is present or absent at the site  $i$ . The evolution equations for the occupation variables  $p_i$  and  $n_i$  are then given by:

$$\begin{aligned}\partial_t n_i &= (1 - n_i - p_i) [r \cdot n_{i+1} + s \cdot n_{i-1}] \\ &\quad - n_i [s \cdot (1 - n_{i+1} - p_{i+1}) + r \cdot (1 - n_{i-1} - p_{i-1})]\end{aligned}\quad (2.8)$$

$$\begin{aligned}\partial_t p_i &= (1 - n_i - p_i) [s \cdot p_{i+1} + r \cdot p_{i-1}] \\ &\quad - p_i [r \cdot (1 - n_{i+1} - p_{i+1}) + s \cdot (1 - n_{i-1} - p_{i-1})],\end{aligned}\quad (2.9)$$

A few comments need to be added to these two equations:

- $r$  and  $s$  are the normalized probabilities, for jumps along and against the field, following from the Metropolis rates (2.1). The normalization factor is absorbed into the time scale. Thus,  $r + s = 1$  with  $r > s$ . Explicitly, they can be written as

$$r = 1/2 + \mathcal{E}/4, \quad (2.10)$$

$$s = 1/2 - \mathcal{E}/4, \quad (2.11)$$

$$\mathcal{E}(E) = 2 \tanh(E/2). \quad (2.12)$$

We refer to  $\mathcal{E}$  as the effective drive which reflects how the microscopic electric field  $E$  enters into the mean field equations, namely, through the relation (2.12).

- The equations of motion for the local occupation variables are directly derived from the master equation (2.2) in one dimension. Two point correlations as  $\langle n n \rangle$  still appear in these equations, but in the spirit of mean-field theory, they are approximated by  $\langle n \rangle \langle n \rangle$ , etc. This leads to the form of Eqs. (2.8) and (2.9).
- A diffusion constant is suppressed here, since it can also be absorbed into the time scale.

Now, we take the continuum limit, i.e., the discrete index  $i$  is replaced by a continuous variable  $y$ . Letting  $p'_i$  denote the derivative of  $p_i$ , we write somewhat formally

$$p_{i\pm 1} = p_i \pm a \cdot p'_i + a^2/2 \cdot p''_i \quad (2.13)$$

$$n_{i\pm 1} = n_i \pm a \cdot n'_i + a^2/2 \cdot n''_i, \quad (2.14)$$

where  $a$  is the lattice constant. All higher order derivatives are neglected. Expressed in terms of the hole density  $\phi(y) = 1 - p - n$  and charge density  $\psi(y) = p - n$ , the two mean field equations now follow:

$$\partial_t \phi = \partial_y \cdot \{ \partial_y \phi + \mathcal{E} \phi \psi \} \quad (2.15)$$

$$\partial_t \psi = \partial_y \cdot \{ \phi \partial_y \psi - \psi \partial_y \phi - \mathcal{E} \phi (1 - \phi) \}. \quad (2.16)$$

In these equations, the lattice constant  $a$  is set to be 1. Searching for a higher-dimensional form of Eqs. (2.15) and (2.16), one has to take into account that the motion of the hole is purely diffusive in the transverse subspace. Extending Eqs. (2.8) and (2.9) by including unbiased ( $q = p = 1/2$ ) jumps in the transverse directions leads to the mean field equations in  $d$  dimensions:

$$\partial_t \phi = \nabla \cdot \{ \nabla \phi + \mathcal{E} \phi \psi \hat{e} \} \quad (2.17)$$

$$\partial_t \psi = \nabla \cdot \{ \phi \nabla \psi - \psi \nabla \phi - \mathcal{E} \phi (1 - \phi) \hat{e} \}, \quad (2.18)$$

where  $\hat{e}$  labels the unit vector in the positive  $y$ -direction.  $\phi, \psi$  are functions on  $d$ -dimensional space, and  $\nabla$  denotes the associated gradient.

In the following, we provide a brief discussion of Eqs. (2.15-2.18), following [17] and [20], to set the scene for our calculation of the order parameter  $Q_L$ . As already pointed out in [17], the mean field equations admit a time-independent homogeneous solution, which is stable to small perturbations provided  $m$  does not exceed a threshold value  $m_H$ , given by

$$m_H = [1 + (2\pi/\epsilon)^2]/2; \quad \epsilon = \mathcal{E}L_y \quad (2.19)$$

These homogeneous solutions reflect the disordered phase. Many quantities in this phase are just constants, e.g.  $\phi_h(y) = 1 - m$  and  $\psi_h(y) = 0$ , trivially derived by integrating the Eqs. (2.15) and (2.16) and using the constraints due to mass and charge conservation (net charge is assumed to be zero). If the lattice is nearly completely filled, i.e., for  $m \lesssim 1$ , the parameter  $\epsilon$  has to be less than  $2\pi$  in order to allow for a stable homogeneous steady state: e.g. considering an electric field  $E = 1.0$ , the system length  $L_y$  has to be very small, namely, less than 7 sites in this case.

To find a steady-state solution which is inhomogeneous in the  $y$ -coordinate only, the time-independent Eqs. (2.15) and (2.16), with left sides set to zero, can immediately be integrated once. The integration constants are the hole and the charge currents. The former vanishes by symmetry at zero total charge. The latter, being non-zero in general, will be denoted by  $j\mathcal{E}$  in the following. After expressing  $\psi$  in terms of  $\phi$  and changing variables to  $z = y/L_y$  and  $\chi = 1/\phi$ , an ordinary differential equation is derived:

$$\chi''(z)/\epsilon^2 = -j\chi^2(z) + \chi(z) - 1. \quad (2.20)$$

Writing  $\chi$  in terms of a potential  $(1/\epsilon^2)\chi'' = -(d/d\chi)V(\chi)$ , a further integration leads to  $\chi' = \epsilon\sqrt{2(U - V)}$ , where  $U$  is another integration constant. Unique periodic solutions exist for  $j < 1/4$  and appropriate  $U$ . Introducing the three roots  $\chi_+, \chi_-$ ,

$\chi_1$ , defined via  $2(U - V(\chi)) = (2j/3)(\chi_+ - \chi)(\chi - \chi_-)(\chi - \chi_1)$ , where  $\chi_1 \leq \chi_- \leq \chi_+$ , the solution [20] can be written using Jacobian elliptic functions [30]:

$$\chi(z) = \chi_+ - (\chi_+ - \chi_-) \operatorname{sn}^2 \left( \epsilon z \sqrt{(j/6)(\chi_+ - \chi_1)} \right). \quad (2.21)$$

in the interval  $0 \leq z \leq 1/2$ . The other half of the interval,  $1/2 \leq z \leq 1$ , is described by symmetry around the axis  $z = 1/2$ . It is convenient to define the parameters  $p$  and  $R$ :

$$p \equiv (\chi_+ - \chi_-)/(\chi_+ - \chi_1) \quad (2.22)$$

$$R \equiv (4K(p)/\epsilon)^2. \quad (2.23)$$

$K$  stands for the complete elliptic integral [30] and is a function of  $p$ . Quantities of interest, such as the mass  $m$  or current  $j$ , can be formulated in terms of  $p$  and  $R$ :

$$1 - 4j = R^2 (1 - p + p^2) \quad (2.24)$$

$$1 - m = \frac{(1 - R^2(1 - p + p^2)) \Pi(n|p)}{2(1 + R + pR) K(p)}, \quad (2.25)$$

where  $\Pi(n|p)$  is the complete elliptic integral of the third kind and  $n$  defined as  $n = 3pR/(1 + R + pR)$ . Functions of interest, e.g.  $j(\epsilon, m)$  or the order parameter  $Q_L(\epsilon, m)$ , can be generated parametrically in  $p$ . For this reason, the allowed values of  $p$  have to be evaluated. Following the discussion in [20],  $p$  ranges from 0 to an upper limit  $p_0(\epsilon) \leq 1$ . Especially  $p_0$  is interesting in the context of this study. It is defined by the vanishing of the current,  $j(\epsilon, p_0) = 0$ . According to Eq. (2.25), the mass density tends towards unity as  $p$  approaches its upper limit  $p_0(\epsilon)$ . Since our study focuses on nearly completely filled systems, only values of  $p$  near  $p_0$  will be of interest here. This observation is used later for approximations.

From the solution for  $\chi(z)$ , the hole density  $\phi = 1/\chi(z)$  and the charge density  $\psi = \chi'/(\epsilon\chi)$  are obtained. Clearly, these solutions describe the ordered phase, i.e., particle-rich strips transverse to the field. With given mass, they depend only on the parameter  $\epsilon = \mathcal{E} L_y$  and the variable  $z = y/L_y$ ; i.e. these functions satisfy scaling in these variables. This is corroborated by the Monte Carlo results of the next Chapter.

Since it is cumbersome to work with the solution 2.21 directly, due to the appearance of the Jacobian elliptic function, its approximation for  $\epsilon \gg 1$  is very useful. The  $\operatorname{sn}$ -function of Eq. (2.21) may be replaced by a  $\tanh$ -function, so that the solution of  $\chi(z)$  is a soliton in the Korteweg–de Vries equation. As a result, a (weak) discontinuity appears in the first derivative of  $\chi$  at the symmetry point  $z = 1/2$ .

This is unfortunate for our purposes, since  $z = 1/2$  is also the location of the maximum hole density. A different approximation, to be presented in the next chapter, resolves this difficulty.

# Chapter 3

## Steady-State Results

### 3.1 Monte Carlo Simulations

The inhomogeneous steady-state configurations are investigated with variable parameters  $E$ ,  $L_x$  and  $L_y$ . In our studies,  $E$  varies between 0.2 and 2.0, while  $L_x$  and  $L_y$  range from 16 to 48. Our “reference system”, which forms the basis for all scaling plots, is characterized by  $E = 0.8$ ,  $L_x = 16$  and  $L_y = 24$ . To provide a visual impression, six snapshots of the reference system, taken at different MC times, are presented in figure 3.1. The minus (plus) particles are colored black (white) and the empty site is marked gray. A coordinate system is introduced in the usual way, i.e., the  $x$ -direction lies horizontal, the  $y$ -direction vertical and the  $E$ -field points upwards.

Starting from a random configuration (Fig. 3.1a), the system remains disordered for early times. Recalling that particles can move only if exchanging with the hole, initially the latter hops through the system without significant effect, leaving the species mixed (fig. 3.1b; 1000 MCS). Eventually, the hole begins to segregate the two species, by allowing positive (negative) particles to move preferentially upwards (downwards). The early stages of this process can be observed in Fig. 3.1c, where an interface between regions of opposite charge begins to develop. In different runs, this interface forms at arbitrary locations, due to random fluctuations in the system. Clearly, due to the periodic boundary conditions, a second interface must also form. After  $10^5$  MCS (Fig 3.1d) the segregation of charges, and hence the two interfaces, are quite apparent. Due to the drive, the hole is driven rapidly to the top (bottom) in regions of predominantly negative (positive) charge. Thus, it tends to remain

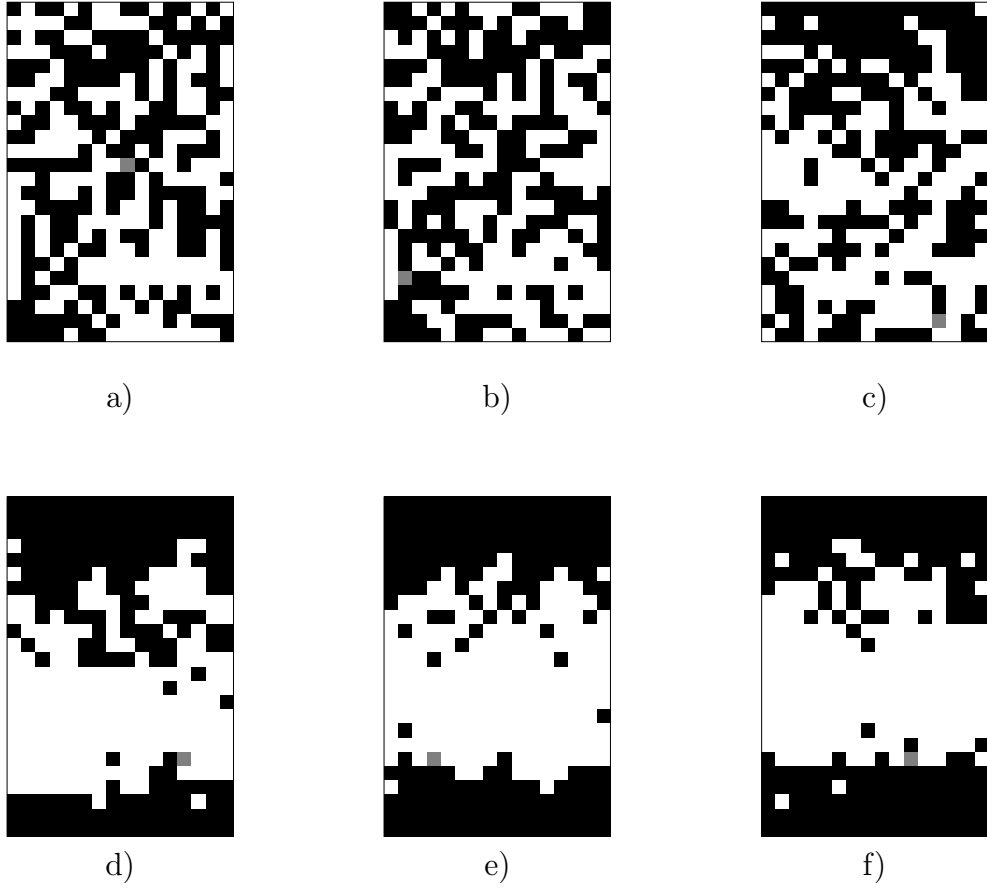


Figure 3.1: Snapshots of an  $L_x \times L_y$  system with  $L_x = 16$  and  $L_y = 24$  at  $E = 0.8$ , at different numbers of MCS: a)1, b) $10^3$ , c) $10^4$ , d) $10^5$ , e) $10^6$ , f) $10^7$ . The initially disordered system undergoes a charge segregation. In the ordered steady-state configuration the two oppositely charged particles are separated by two different interfaces. Minus particles are colored black, plus white and the hole is gray.  $E$ -field and  $y$ -direction point upwards.

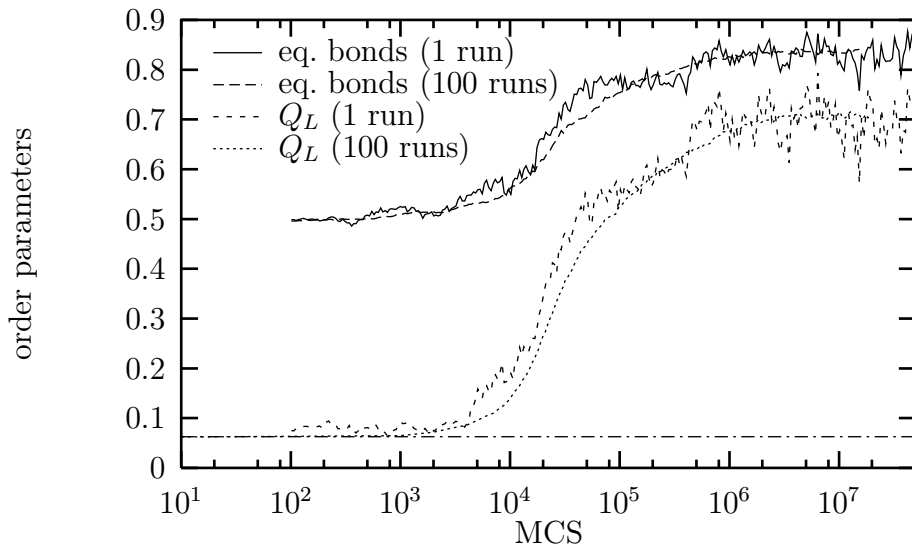


Figure 3.2: Half logarithmic plot of order parameters, for a system with  $L_x = 16$ ,  $L_y = 24$  and  $E = 0.8$ . The two upper curves show the number of equal neighbor bonds normalized by the total number of bonds; the lower curves show the order parameter  $Q_L$ . The smoother curves are averages over 100 runs, the rougher ones show a single run. The straight dashed-dotted line is the constant  $1/L_x$ .

near the interface which separates positive particles on the top from negative ones on the bottom (the lower interface in Figs. 3.1d-f). In contrast, it is rapidly driven away from the opposite interface. We will refer to the former (latter) interface as the “downstream” (“upstream”) one. Clearly, the morphologies of the two interfaces are rather different. Whereas the downstream interface is rather sharp and smooth, the upstream interface appears to be much more diffuse. To increase the degree of order in the system, the hole has to travel to the upstream interface through a series of field-suppressed jumps, before it can move another charge to a preferred position. As the ordered domain surrounding the downstream interface grows, the hole becomes even more localized. Thus, the system approaches the final steady state very slowly. A picture of a typical steady-state configuration is shown in Fig. 3.1f.

The order parameter  $Q_L$ , Eq. (2.7), is shown in the two lower curves of Fig. 3.2. The smoother line is an average over 100 runs whereas the other one represents the single run displayed in Fig. 3.1. Four different regimes can be identified. In the initial, earliest regime the order parameter remains nearly constant at the finite size value  $1/L_x$  (see Sec. 2.2), which is marked by the straight line. In the second regime (here:  $\approx 5 \times 10^3 - 10^5$  MCS), the segregation process starts. After a strip of two

ordered regions, one consisting of positive and the other one of negative charges, has formed in the system, the order parameter grows more slowly by broadening the strip (third regime, here:  $\approx 10^5 - 5 \times 10^6$  MCS). Finally, the steady state is reached in the last regime, and the order parameter has saturated, exhibiting only steady-state fluctuations.

The standard deviation is calculated to  $\pm 0.03$  for MC-times less than 1000, averaging over 100 sample runs. In the second and third regime, where the order parameter increases, the standard deviation is about  $\pm 0.05$  and finally, it is about  $\pm 0.04$  in the saturation regime. However, we should note, that the standard deviation is dependent on the parameters.

An alternative measure of the ordering process is presented in the upper two curves of Fig. 3.2. The number of bonds between equal nearest neighbors is counted and normalized by the total number of bonds on the lattice (here:  $2 \cdot (16 \times 24) = 768$ ). Clearly, the initial value of this quantity is  $1/2$  since the initial configuration is random. Otherwise, its behavior is qualitatively similar to that of  $Q_L$ . However, in the following, we will focus on  $Q_L$ , since it is more easily computed in the frame of mean field theory (see Sec. 3.2). As a remark, the charge current, used in ref. [20], is unsuitable as an order parameter in this study. Because of the high mass density in the system, the current almost vanishes.

Here, we turn our attention towards the characterization of the saturated regime, i.e., the steady states. The ordering process and its dynamic scaling properties form the subject of further studies which will be published later elsewhere [31]. Nevertheless, we should mention that the ordering process may be more complicated at higher  $E$ -fields and in systems with larger  $L_y$ , i.e., for  $\epsilon = \mathcal{E} L_y \gtrsim 24$ . In such systems, multiple strips are likely to occur which have a major effect on the time dependence of the order parameters. However, even if multiple strips appear in the ordering process, the steady state consists only of two charge-segregated regions separated by two interfaces, at least for the values of  $\epsilon$  considered here ( $\epsilon \lesssim 30$ ).

## 3.2 Scaling of the Order Parameter

Focusing on the steady state, we measure the associated order parameter  $Q_L$  and plot it in Figure 3.3, for a range of system sizes and electric fields, near complete filling. As the discussion in Sec. 2.5 illustrates, the steady-state solution for the charge density profile  $\psi$  satisfies scaling in  $\epsilon = \mathcal{E} L_y$ . Thus, we expect  $Q_L$ , being

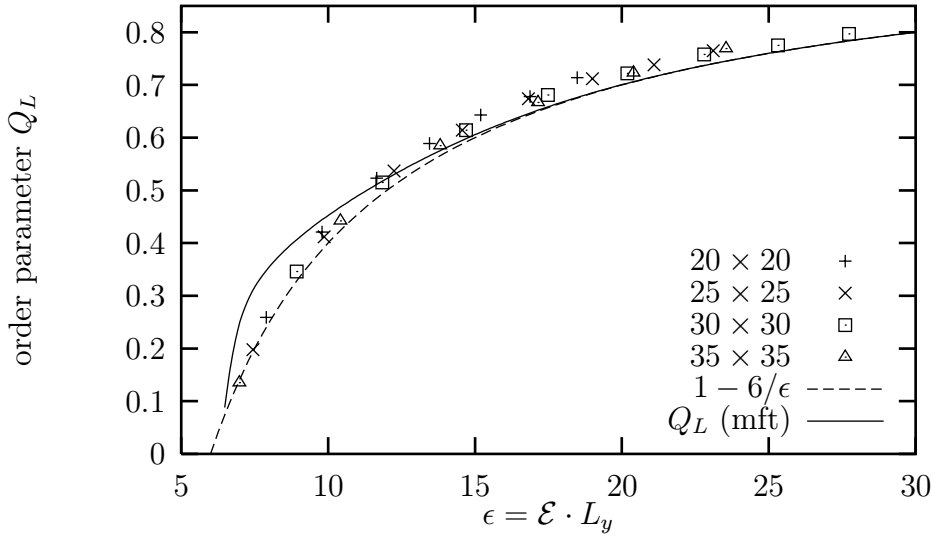


Figure 3.3: Plot of order parameter vs  $\epsilon$  for different square system square sizes ( $20 \leq L_x = L_y \leq 35$ ) and different electric fields ( $0.2 \leq E \leq 1.0$ ). The upper line shows the result of  $Q_L$  from mean field theory, the lower line is its approximation  $1 - 6/\epsilon$ .

defined entirely in terms of this profile, to depend only on the scaling variable  $\epsilon$ , which is borne out by Figure 3.3. The data points in the plot are results of Monte Carlo simulations for different square systems (ranging from  $20 \times 20$  to  $35 \times 35$ ) and different electric fields ( $E = 0.2$  to  $1.0$ ), each averaged over 30 – 50 runs. Within the accuracy of our data, all points lie on the same curve, corresponding to the scaling function. The latter appears to tend towards zero for small values of  $\epsilon$  ( $\gtrsim 6$ ). This is consistent with the stability limit of the inhomogeneous solutions, Eq. (2.19), which implies that for  $m \approx 1$ , an inhomogeneous solution can exist only if  $\epsilon > 2\pi$ . Once the transition to the homogeneous phase has occurred, the order parameter is of the order of  $1/L_x \leq 0.05$ . With increasing  $\epsilon$  the order parameter approaches its upper limit, i.e., 1.

Aiming to establish a parallel to the simulation results, we now calculate the order parameter  $Q_L$  in a mean field approximation. First,  $Q_L$  needs to be written in the continuum limit. The summation over the sites in the  $y$ -direction is replaced by an integration. Using the variable  $z = y/L_y$ , the integration runs over the whole system size, i.e., from zero to one:

$$Q_L = \frac{1}{m} \int_0^1 [\psi(z)]^2 dz. \quad (3.1)$$

Since the charge density  $\psi$  is odd around  $z = \frac{1}{2}$ , this is equal to twice integrating over the interval zero to one half. Writing  $\psi$  in terms of the hole density for which holds  $\phi = 1/\chi$  (cf. discussion above Eq. (2.20)), the equation

$$Q_L = \frac{2}{m \epsilon^2} \int_0^{1/2} \frac{\chi'^2}{\chi^2} dz \quad (3.2)$$

is derived. One could now insert the explicit solution for  $\chi(z)$ , but the integration over  $z$  turns out to be very difficult. For this reason, the integration variable is changed to  $\chi$ ; then, we integrate from  $\chi_-$  to  $\chi_+$ . Expressing the integrand in terms of the three roots  $\chi_1, \chi_-, \chi_+$  (see the discussion below Eq. (2.20)) and reducing terms higher than  $\chi^2 \chi'$ , it can be written in terms of two trivial integrals and two elliptic integrals.

$$Q_1 = - \int_{\chi_-}^{\chi_+} \frac{\chi}{\chi'} d\chi \quad (3.3)$$

$$Q_2 = (\chi_1 \chi_- \chi_+) \int_{\chi_-}^{\chi_+} \frac{1}{\chi^2 \chi'} d\chi \quad (3.4)$$

$$Q_3 = (\chi_1 + \chi_- + \chi_+) \int_{\chi_-}^{\chi_+} \frac{1}{\chi'} d\chi \quad (3.5)$$

$$Q_4 = -(\chi_+ \chi_- + \chi_+ \chi_1 + \chi_- \chi_1) \int_{\chi_-}^{\chi_+} \frac{1}{\chi \chi'} d\chi; \quad (3.6)$$

with  $Q_L = \frac{4j}{3m}(Q_1 + Q_2 + Q_3 + Q_4)$ . The last two integrals are evaluated easily, giving  $1/2$  and  $(1 - m)/2$ . The first two integrals are more difficult, but it is possible to compute them in terms of complete elliptical integrals of the first, second and third kind. The lengthy expressions are omitted here. To express the result for  $Q_L$  in more compact form, using the parameters  $m, p$  and  $R$  (see Eqs. (2.22) and (2.23)), it is helpful to write the three roots in terms of  $p$  and  $R$

$$\chi_1 = \frac{2(1 + R(p - 2))}{1 - R^2(1 - p + p^2)} \quad (3.7)$$

$$\chi_- = \frac{2(1 + R(1 - 2p))}{1 - R^2(1 - p + p^2)} \quad (3.8)$$

$$\chi_+ = \frac{2(1 + R(1 + p))}{1 - R^2(1 - p + p^2)} \quad (3.9)$$

Finally, we invoke Eq. (2.24) to substitute the current  $j$  and Eq. (2.25) to replace the elliptic integral of the third kind. Collecting, we obtain  $Q_L$ :

$$Q_L = 1 - \frac{1}{2m} \left\{ R(p - 2) + 1 + 3R \frac{E(p)}{K(p)} \right\}. \quad (3.10)$$

$E$  and  $K$  are the complete elliptical integrals of the first and second kind [30]. The mass density  $m$  can be replaced by Eq. (2.25), so that the order parameter is only a function of  $p$ ,  $R$  and  $\epsilon$ . Recalling that that  $R$  has been defined in Eq. (2.23),  $Q_L$  becomes a function of  $p$  and  $\epsilon$  only.

For a given mass density  $m$  and a given  $\epsilon$ , the parameter  $p$  is determined in principle by Eq. (2.25). In practice, it is not possible to invert this equation; however, as mentioned in Sec. 2.5, the order parameter can be plotted parametrically in  $p$ , remaining a function of  $\epsilon$  only.  $p$  takes values in the interval  $[0, p_0(\epsilon)]$  (cf. the discussion below Eq. (2.25)).

In the limit  $p \rightarrow 0$ , Eq. (2.25) shows that  $m$  approaches the stability limit (2.19), i.e.,  $m \rightarrow (1+R)/2$ . Here, the complete elliptic integrals approach the limiting value  $\pi/2$ . Thus, the order parameter vanishes in this limit.

The other limit,  $p \rightarrow p_0(\epsilon)$ , defined through  $j(\epsilon, p_0(\epsilon)) \rightarrow 0$ , corresponds to the case that is of interest here, namely,  $m(p_0(\epsilon)) \rightarrow 1$  (see Eq. (2.25)). Clearly, our goal is to find  $Q_L(\epsilon, m)$ , while Eq. (3.10) gives us only  $Q_L(\epsilon, p)$ . Thus, we need to determine  $p_0(\epsilon)$ . Noting that Eq. (2.24), for  $j = 0$ , can be rewritten as  $\epsilon^2 = [4K(p_0)]^2(1 - p_0 + p_0^2)$ , we can compute  $\epsilon$  numerically for a set of discrete values of  $p$  in the interval  $[0, 1]$ . The values of  $Q_L(\epsilon, m = 1)$ , derived in this way, are plotted in Fig. 3.3.

For large  $\epsilon \gg 1$ , the approximations  $R \simeq \sqrt{1-4j}$  and  $p \simeq 1$  are valid. Expressing the roots  $\chi_1, \chi_-, \chi_+$  and the integrals of Eqs. (3.3–3.6) with the help of these approximations,  $Q_L$  simplifies to:

$$Q_L = 1 - \frac{1}{m} \left\{ \frac{6}{\epsilon} + j \left( 1 - \frac{6}{\epsilon} \right) \right\}. \quad (3.11)$$

Within the same approximation,  $j$  can be replaced by  $j = \exp(-m\epsilon/2)$  [20]. For large  $\epsilon$  and finite  $m$ , this term is vanishingly small compared to the other terms in  $Q_L$ , so that

$$Q_L = 1 - \frac{6}{m\epsilon} \quad (3.12)$$

to excellent accuracy, which is plotted in Fig. 3.3, with  $m$  set to one.

For  $\epsilon > 18$ , this approximation is not distinguishable from the exact  $Q_L(\epsilon, 1)$ , as demonstrated by Fig. 3.3. For smaller values of  $\epsilon$ , the approximation underestimates the order parameter slightly. It is remarkable, however, that the simulation data appear to fit the approximation better than the exact mean field result, especially for  $\epsilon < 10$ . It is conceivable that the intrinsic errors of the mean-field theory approach

are partially compensated by the large  $\epsilon$  limit. Further studies are required to test this conjecture. Finally, focusing on the region  $\epsilon > 15$ , the simulation results all lie about 0.02 units above the theoretical curve, which is within the error bars ( $\approx 0.05$ ). Closer scrutiny reveals that the results of the large system sizes tend to be closer to the theoretical curves than those for small system sizes, which indicates that the divergence of simulation and mean field results is at least partly caused by finite size effects. The major reason for the divergence, however, becomes more clear in the context of Sec. 3.5.

### 3.3 Scaling of the Charge and Hole Density

While the order parameter carries only global information about spatial inhomogeneities in the system, the charge and hole density profiles retain far more detail, allowing us to distinguish the oppositely charged domains and their interfaces. Based on the mean-field theory presented in Sec. 2.5 and in [20], we expect these densities to satisfy scaling in  $\epsilon$  and  $z$ . This is borne out by the simulations results which are presented in this Section.

In order to exhibit the scaling of the densities, four different simulations, consisting of 100 runs each, were performed, with varying system length  $L_y$  and electric field  $E$ , keeping the parameter  $\epsilon$  constant. Starting from a lattice with  $L_x = 16$  and  $L_y = 24$ , we increase  $L_y$  in steps of 8 to a maximum of 48 sites, whereas  $L_x$  remains fixed. Simultaneously, the electric field  $E$  is decreased from 0.8 to 0.586, then 0.464 and finally 0.385 in the different simulations. Thus,  $\epsilon = \mathcal{E} \cdot L_y$  remains constant at the value 18.24. Clearly, starting from a random initial configuration, the charged strips form at random positions in the system. To avoid unwanted cancellations when averaging profiles from different runs, we shift the maximum of the hole density in each run to  $z = 0$  before averaging. Referring to the discussion in Sec. 3.1, this implies that the “downstream” interface is centered at the origin. The charge profiles are shifted accordingly. Thus,  $z$  covers the interval  $(-0.5, 0.5)$ . In addition, we normalize the hole profile in such a way that all profiles enclose the same area.

A comment on this normalization is in order. First, we recall the constraint on the total density,  $1 - m = (1/L_y) \int_0^{L_y} \phi(y) dy$ . According to Eq. (2.4),  $1 - m = 1/(L_x L_y)$  for a single hole. Thus, we have  $1 = L_x \int_0^{L_y} \phi(y) dy = L_x L_y \int_0^1 \phi(z) dz$  so that  $L_x \phi(y)$  can be interpreted as the *probability density* for finding the hole in row  $y$ . Similarly,  $L_x L_y \phi(z)$  is the probability density for finding the hole at position  $z$ . Thus, *normalized* plots for the hole density show the associated probability density,

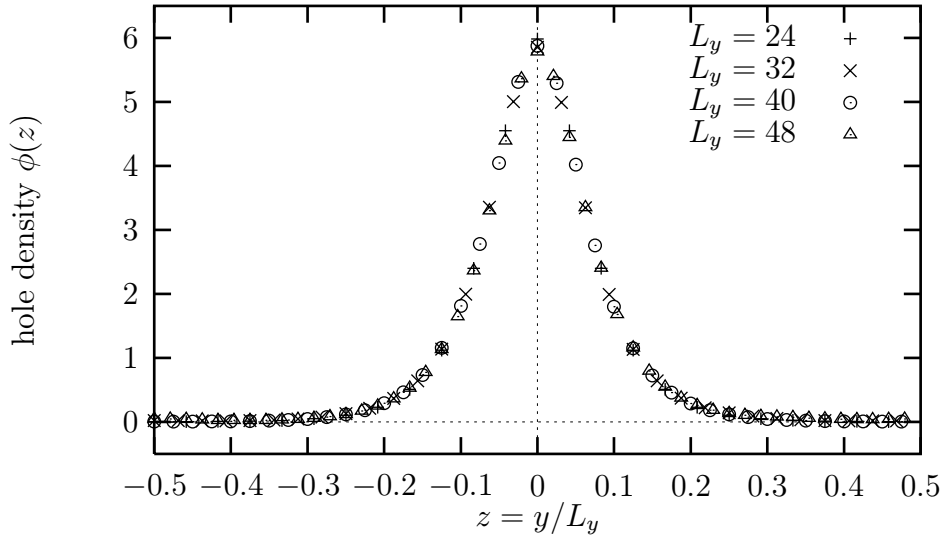


Figure 3.4: Scaling plot of the hole density.  $L_y$  and  $E$  vary such that  $\epsilon = 18.24$  remains constant.  $L_x = 16$  is fixed.

and the area under each curve is just 1. No such normalization is required for the charge density, since its integral equals zero.

The results for the hole density profile are presented in Fig. 3.4 and the charge density profile is shown in Fig. 3.5. Clearly, all data points collapse onto the same characteristic scaling curve for hole and charge profiles, respectively, confirming the theoretical prediction.

Beyond demonstrating scaling, these plots provide a more quantitative characterization of the spatial structures in the system than the qualitative description in Sec. 3.1. Since  $\epsilon$  here is the same as in Figs. 3.1a-f, Fig. 3.5 shows the associated steady-state charge density profiles. We can see clearly that the particles are ordered in two regions, filling the whole system. Each of these regions consists essentially of one species. They are separated by two interfaces. The maximum of the hole density lies at the center ( $z = 0$ ) of the much sharper “downstream” interface where the field tends to localize the hole, while the minimum of the hole density marks the more diffuse “upstream” interface.

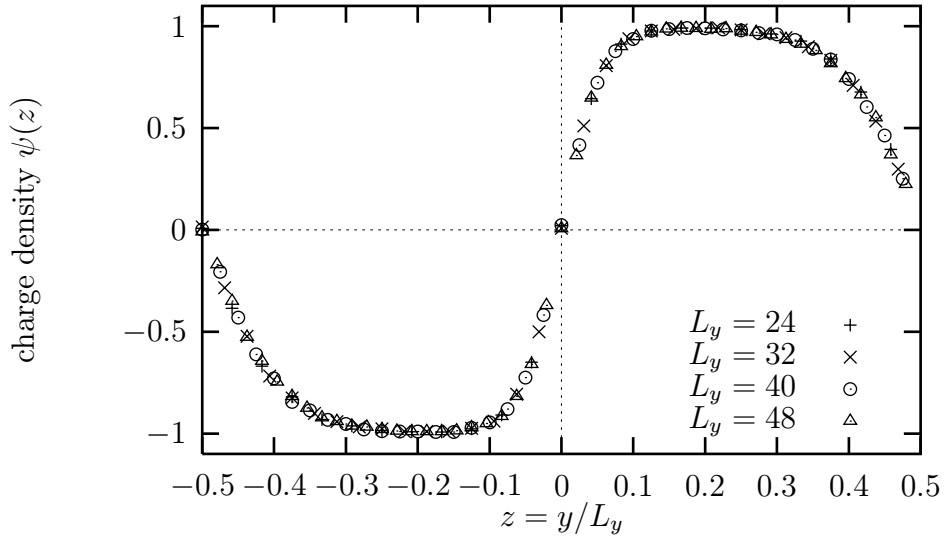


Figure 3.5: Scaling plot of the charge density, at the same parameter values as Fig. 3.4.

### 3.4 Size and Field Dependence of Charge and Hole Density

To explore the size- and field-dependence of our system further, it is interesting to vary the system length  $L_y$  and the electric field  $E$  independently, without keeping  $\epsilon$  constant. Focusing on the spatial inhomogeneities which form along the  $y$ -direction, the system size  $L_x$  is not expected to have an influence on steady-state observables such as the hole and charge densities or the order parameter. Simulations confirm this, provided the aspect ratio  $L_x/L_y$  does not exceed a certain threshold value which is at least 6 in our case. For larger aspect ratios, strip configurations with nonzero winding number may begin to form, introducing an  $L_x$ -dependence into the problem [18].

#### 3.4.1 Simulations with varying $L_y$

We first report simulations at constant electric field  $E = 0.8$  and transverse size  $L_x = 16$ , increasing the longitudinal system size  $L_y$  from 20 to 32 in steps of 4. The hole densities observed in these simulations are summarized in Fig. 3.6, plotted vs

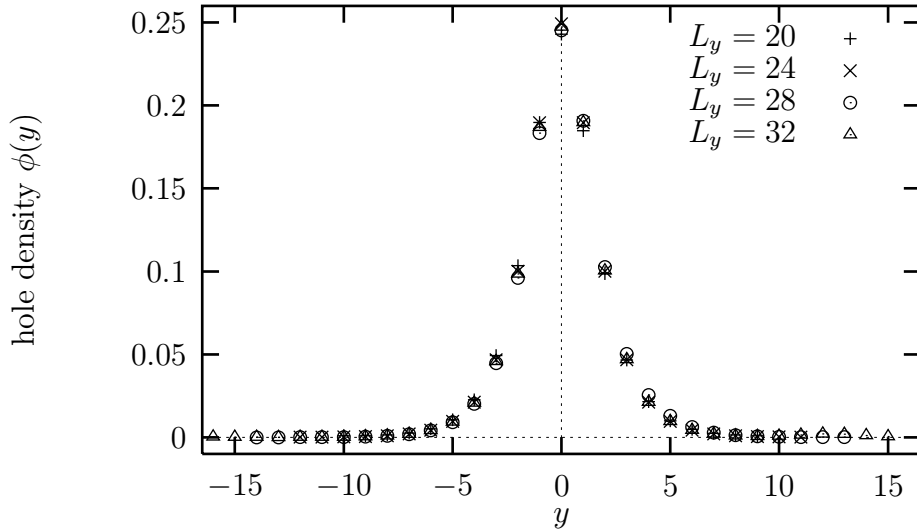


Figure 3.6: Plot of the hole density for a range of  $L_y$ .  $L_x = 16$  and  $E = 0.8$  are constant.

$y$  rather than  $z = y/L_y$ . The areas under the different curves are normalized to one (cf. comment on normalization in Sec. 3.3).

We observe that the graphs associated with different  $L_y$  span different ranges of  $y$ , but are otherwise essentially indistinguishable in the central region. As a result, we conclude that the width and the maximum of the hole density, and hence the width of the “downstream” interface, are not affected by changes in the longitudinal system size when plotted vs the  $y$ -variable. Thus, we may conclude further that the characteristics of the interface are controlled by the electric field alone (cf. next section).

This behavior is also borne out by the charge density profiles, Fig. 3.7. According to our mean-field equations of motion, (2.15) and (2.16), the steady-state charge and hole density profiles are related via  $\psi(y) = -\phi'(y)/(\mathcal{E}\phi(y))$ . Thus, the charge densities near the “downstream” interface should also be independent of  $L_y$ , in agreement with Fig. 3.7. On the other hand, the regions of nearly constant charge density must broaden, to reflect the increasing system size. We should emphasize that this is not a contradiction to our mean-field relation, since both  $\phi'(y)$  and  $\phi(y)$  are very small outside the central region, i.e.,  $-5 \lesssim y \lesssim 5$ , so that any  $L_y$ -dependence is not easily observed. However, a plot of the charge densities locating the upstream interface at  $y = 0$  indicates that the upstream–interfacial region is

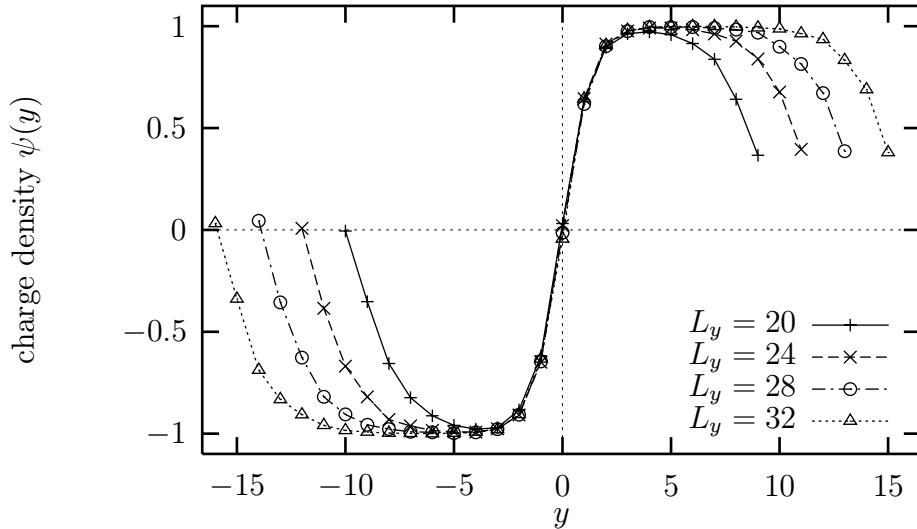


Figure 3.7: Plot of the charge density, at the same parameters as Fig. 3.6

also independent of  $L_y$ , i.e., the width and slope is not affected by  $L_y$ . Since the plot does not contain any new information, it is omitted here. Instead, a charge density plot of the upstream interface is presented in the next section (Fig. 3.9). To summarize, both interfaces, plotted vs  $y$ , are independent of system size.

### 3.4.2 Simulations with different $E$

In this section, all parameters are held constant except the field  $E$  itself, in order to clarify how the density profiles depend on the electric field. In our Monte Carlo simulations, the system size is now fixed at  $L_x \times L_y = 16 \times 24$ , while the electric field increases from 0.4 to 1.2 in steps of 0.2. In Fig. 3.8, the hole density profile is plotted vs the scaling variable  $\mathcal{E}y$ , and the area under the different curves has again been normalized. Under these condition, the data for  $E \geq 0.6$  collapse onto a single scaling curve. The smallest  $E = 0.4$ , in contrast, shows systematic deviations from scaling. We should note, however, that this value of  $E$  is rather close to the transition to the homogeneous phase where the mean-field theory is likely to break down. Near the transition, the hole density becomes less sharply peaked and the two interfaces are no longer so well separated from one another. For the larger values of  $E$  considered here this is not the case. Instead, near the central region the data for these  $E$  collapse onto a single curve. This indicates that the *width* of the

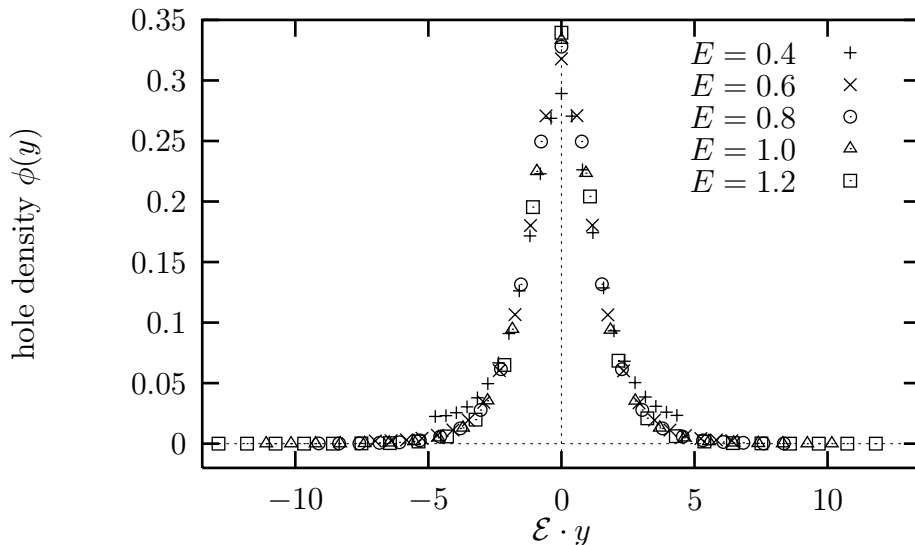


Figure 3.8: Plot of the hole density vs  $\mathcal{E}y$ , for a  $16 \times 24$  system. The  $E$ -field is varied.

downstream interface scales as  $1/\mathcal{E}$ , i.e., at least within this region,  $\phi$  depends on  $y$  via the combination  $\mathcal{E}y = \epsilon z$ . Turning to the charge densities, we invoke the steady-state relation  $\psi(y) = -\phi'(y)/(\mathcal{E}\phi(y))$ . The characteristic  $y$ -dependence of  $\phi$  implies that  $\psi(y)$  is also a function of  $\mathcal{E}y$ , (note that the  $\mathcal{E}$  in the denominator cancels with the derivative). Thus, we expect  $\psi$  to scale near the downstream interface also. Indeed, this scaling can be confirmed by a plot of  $\psi$  similar to Fig. 3.8. To remain brief, we omit this plot and consider the upstream interface instead.

Focusing on the upstream interface, located at the minimum of the hole density, it is difficult to make a statement for the charge density, based on Fig. 3.8 since both  $\phi$  and its slope are extremely small there. To remedy this situation, we shift the upstream interface to the origin. Thus, in Fig. 3.9, the charge densities are presented, such that the graphs are shifted by half the system length  $L_y$  compared to Fig. 3.8. Remarkably, it is quite clear that this interface also scales in the variable  $\mathcal{E}y$ .

Let us summarize the key findings of the simulations. First, the data for each profile collapse onto a single scaling curve if plotted as a function of  $z = y/L_y$  at constant  $\epsilon$ . Moreover, using  $y$  as variable, we find that *both* interfaces are independent of  $L_y$  and that their widths scale as  $1/\mathcal{E}$ , provided we are not too close to the transition to the homogeneous phase. In the next section, we will consider these

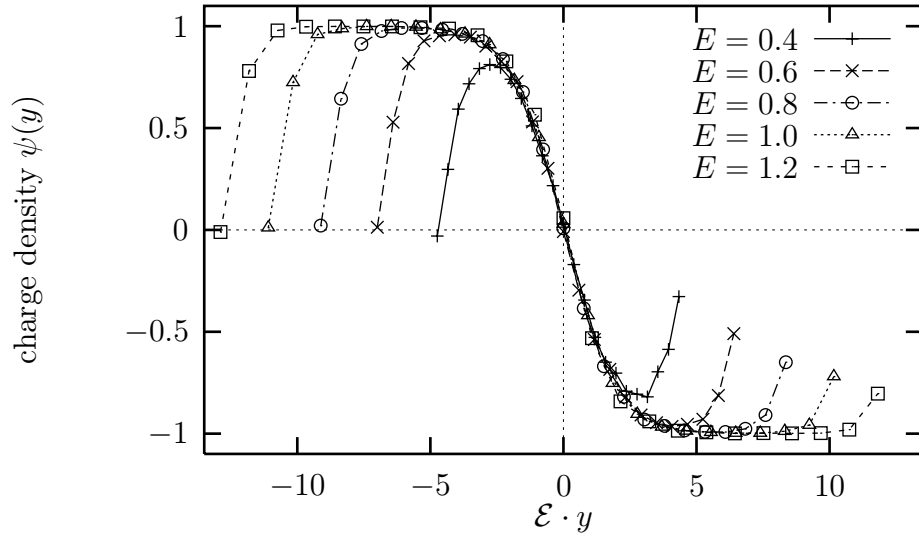


Figure 3.9: Plot of the charge density vs  $\mathcal{E} y$ , for the same system as Fig. 3.8. Note that  $y = 0$  corresponds to the *minimum* of the hole density here (upstream interface).

findings in the light of our mean-field theory.

### 3.5 Independent Interface Approximation

In this section, we first present an analytical description of the interfaces which is then tested by rather detailed Monte Carlo simulations. We will focus in particular on the charge density since it directly determines the order parameter. First, we invoke the “large  $\epsilon$ ” approximation [20] to describe the upstream interface where the hole density has its minimum. A complementary approximation, involving a different version of the large  $\epsilon$  limit, is then developed to describe the other (downstream) interface. The key assumption here is that the two interfaces are independent from one another, i.e., they are separated by sufficiently large regions which are entirely filled by either positive or negative charges. Such profiles result if the parameters for the simulations are chosen such that  $\epsilon \gtrsim 18$ . This is demonstrated by Figs. 3.5, 3.7 and 3.9, where the charge density is essentially  $\pm 1$  away from the interfacial regions. Moreover, Figs. 3.4, 3.6 and 3.8 exhibit that, for large  $\epsilon$ , the hole density is approximately zero away from the downstream ( $z = 0$ ) interface.

Next, we consider our mean-field theory for large  $\epsilon$ . Recalling Sec. 2.5 and 3.2, taking the large  $\epsilon$  limit is equivalent to  $p \rightarrow 1$ . In this limit, we can replace the Jacobian elliptic function  $\text{sn}$  by  $\tanh$  [20]. In practice, this is already a good approximation for  $\epsilon \geq 15$ . Note that this results in (mean-field) profiles with vanishing hole densities near the upstream interface and saturated charge densities between the interfacial regions. Thus, this limit is consistent with our assumption of “independent” interfaces.

To describe the upstream interface, we can simplify Eq. (2.21) for large  $\epsilon$ :

$$\chi(z) = \chi_+ - (\chi_+ - \chi_-) \tanh^2(\epsilon z/2) \quad (3.13)$$

Note that, due to the symmetry of  $\chi$ , this equation holds for the interval  $(-1/2, 1/2)$ . Here,  $\chi = 1/\phi$  takes its maximum at  $z = 0$ , so that this is a good approximation for the upstream interface. The largest deviation from the exact mean-field solution occurs at the boundaries, i.e., near the downstream interface, since our approximation does not satisfy periodic boundary conditions, i.e.,  $\chi'(-1/2) = -\chi'(1/2)$ . Therefore, we introduce a different approach for the downstream interface below. The current is exponentially suppressed for large  $\epsilon$ , i.e.,  $j \cong 6 e^{-m\epsilon/2}$ , and  $\chi_+$  and  $\chi_-$  can be expressed in terms of  $j$ , namely,  $\chi_+ - \chi_- \cong \frac{3}{2j} \sqrt{1 - 4j}$  and  $\chi_+ \cong \frac{1}{2j} (1 + 2\sqrt{1 - 4j})$ . Now, the equations for the hole and charge densities can be easily derived. In particular, recalling that  $y = L_y z$ , we can already read off the width  $\xi_u$  of the upstream interfacial region as  $\xi_u = 2L_y/\epsilon = 2/\mathcal{E}$  which is consistent with the data. More specifically, the charge density is given by  $\psi(z) = \chi'(z)/(\epsilon \chi(z))$ . Computing the

derivative from Eq. (3.13), and neglecting terms of  $O(j)$ , we find

$$\psi(y) = -\tanh(\mathcal{E} y/2). \quad (3.14)$$

The variables  $y$  and  $\mathcal{E}$  are more convenient in order to compare Eq. (3.14) with the simulation results. At the boundaries, Eq. (3.14) results in  $\psi(\pm L_y/2) \rightarrow \mp 1$  in the large  $\epsilon$  limit, which demonstrates again that our approximation violates the boundary condition when considering the whole system. However, it does describe the interfacial region near  $y = 0$  very well. Rather than quoting the hole density explicitly, we only note that it is very small near the origin, namely  $O(j)$ .

In order to capture the downstream interface, we introduce another method. Since  $j \cong 0$  to excellent accuracy for large  $\epsilon$  [20], we return to the two mean-field Eqs. (2.15) and (2.16) and integrate them, setting *both* integration constants, i.e., hole *and* charge current, to zero. This is an equilibrium approximation (see below). In the variables  $y$  and  $\mathcal{E}$ , the boundary conditions are chosen as  $\phi(\pm L/2) \rightarrow 0$  and  $\psi(\pm L/2) \rightarrow \pm 1$ . In this approximation, the downstream interface, corresponding to the maximum of the hole density, is localized at the origin. Following the same steps as in Sec. 2.5, we express  $\psi$  in terms of  $\phi$  and substitute into Eq. (2.16). This results in an ordinary differential equation for  $\chi(y)$ :  $\chi'' - \mathcal{E}^2 \chi + \mathcal{E}^2 = 0$ , which is easily solved:

$$\chi(y) = c_1 e^{\mathcal{E}y} + c_2 e^{-\mathcal{E}y} + 1. \quad (3.15)$$

Since  $\chi$  should be even in  $y$ , the two integration constants must be equal,  $c_1 = c_2 = c$ . For sufficiently large  $\epsilon$ , both boundary conditions on  $\phi$  and  $\psi$  are satisfied. Additionally, they fix  $c > 0$ . To determine  $c$  explicitly, we use the constraint on the hole density, namely  $1 = L_x \int_{-L_y/2}^{L_y/2} \phi(y) dy$ . Integrating the hole density  $\phi(y) = 1/\chi(y)$ , we obtain in the large  $\epsilon$  limit:

$$2 \frac{L_x}{\mathcal{E}} \frac{1}{\sqrt{4c^2 - 1}} \arccos\left(\frac{1}{2c}\right) = 1 \quad (3.16)$$

whence  $c > 1/2$  follows. From Eq. (3.16), a solution for  $c$  is provided by asymptotic expansions of the square root ( $\sqrt{4c^2 - 1} \cong 2c - 1/(4c)$ ) and of the arccos-function ( $\arccos\left(\frac{1}{2c}\right) \cong \frac{1}{2}\pi - \frac{1}{2c}$ ). Then,

$$c = \frac{\pi L_x}{2 \mathcal{E}} - \frac{1}{\pi} \quad (3.17)$$

Both asymptotic approximations are already very good if  $c$  exceeds 2 which is the case in all our simulations since inserting our smallest  $L_x = 16$  and the highest  $\mathcal{E} \rightarrow 2$  results in  $c > 12$ . Next, we compute the charge density,

$$\psi(y) = \frac{e^{\mathcal{E}y} - e^{-\mathcal{E}y}}{e^{\mathcal{E}y} + e^{-\mathcal{E}y} + 1/c} = \frac{\sinh(\mathcal{E}y)}{\cosh(\mathcal{E}y) + 1/(2c)} \quad (3.18)$$

where  $c$  is determined by Eq. (3.17). To simplify Eq. (3.18), we recall  $c > 12$  and approximate, to very good accuracy

$$\psi(y) \simeq \tanh(\mathcal{E} y). \quad (3.19)$$

Again, we can read off the width of the interfacial region,  $\xi_d = 1/\mathcal{E}$ . Similar to the downstream interface, the width scales with  $1/\mathcal{E}$ , in agreement with the data. Intriguingly, however, our approximation is capable of reproducing the observation that the downstream interface is *narrower* than the upstream one. Whether the measured widths differ by a simple factor of 2, as predicted by our calculation, awaits a more quantitative comparison with Monte Carlo data.

In contrast to the upstream interface where the hole density was  $O(j)$ , here  $\phi$  provides more information,

$$\phi(y) = \frac{1}{1 + 2c \cosh(\mathcal{E}y)} \simeq \frac{1}{2c \cosh(\mathcal{E}y)} \quad (3.20)$$

in the large  $c$  limit, with  $c$  given by Eq. (3.17), confirming the width of the downstream interface  $\xi_d = 1/\mathcal{E}$ . Away from the origin, the hole density again decays very rapidly, to match with its value near the upstream interface.

Before turning our focus on a comparison of these results with computer simulations, a last remark on the approximation of the downstream interface is in order. Defining brick-wall boundary conditions in our model instead of periodic ones, the approximation taken here (setting the current to zero) becomes exact. Moreover, the “brick-wall” system is an *equilibrium* one. The hole will segregate the positive (negative) charged particles to the top (bottom) “wall” of the system, thus establishing our boundary condition  $\psi(\pm L/2) \rightarrow \pm 1$ . Finally, only one nontrivial interface remains in the system, namely, the downstream one. In the steady state, the bias traps the hole near this interface. This fixes the boundary condition  $\phi(\pm L/2) \rightarrow 0$ . Both boundary conditions were part of our approximation scheme for the downstream interface. In that sense, our approximation for the downstream interface is equilibrium-like.

Returning to the case of periodic boundary conditions, we present a brief summary of our results so far. Two compact equations, (3.14) and (3.19), are derived for the charge density. Since  $\psi(y) \simeq \pm 1$  between the interfaces, to excellent accuracy, the whole system can be described in terms of the two interfaces. As an example, we consider a  $16 \times 24$  system with  $E = 0.8$  in Fig. 3.10. The data points are obtained from a direct computer simulation while the lines reflect our two interface approximations, Eqs. (3.14) and (3.19). For the narrower interface (in the center of the

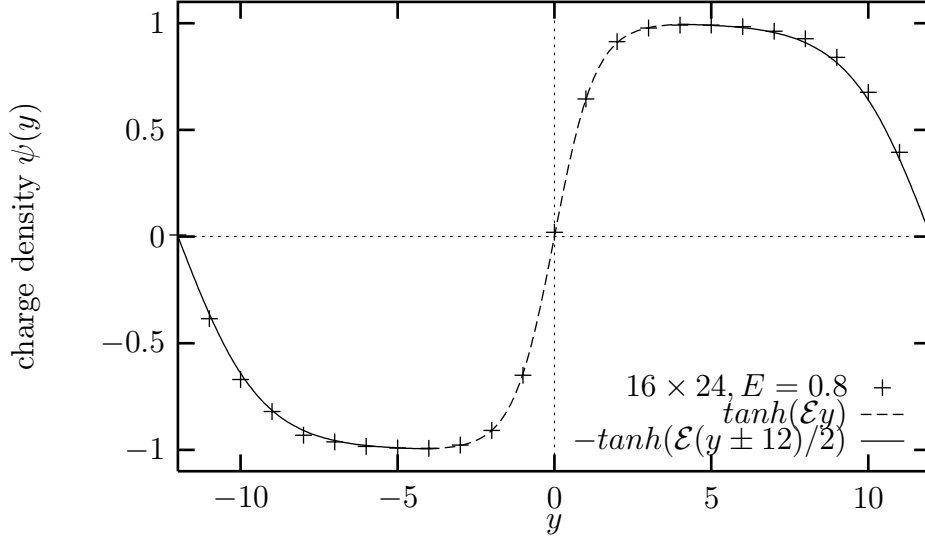


Figure 3.10: Plot of the charge density (+) for  $L_x = 16$ ,  $L_y = 24$  and  $E = 0.8$ . The dashed and solid lines are the two interface approximations, Eqs. (3.14) and (3.19), matched at  $y = \pm 4$ .

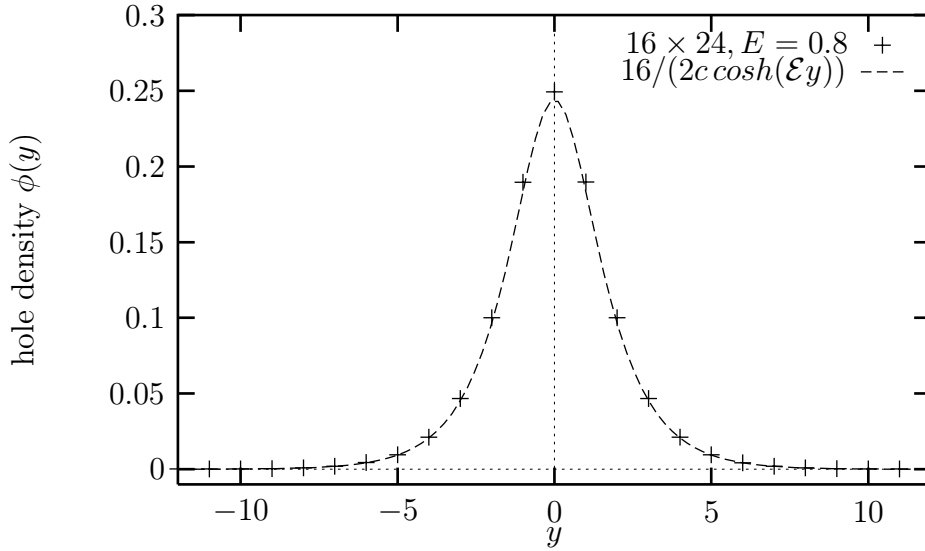


Figure 3.11: Plot of the hole density (+) for  $L_x = 16$ ,  $L_y = 24$  and  $E = 0.8$ . The dashed line denotes the approximation (3.20) for the downstream interface, with  $c = 32.79$ . Note that the hole density is vanishingly small near the upstream interface.

picture), the match is nearly perfect, while for the wider interface (at the boundaries of the figure) the slope of the tanh–function is slightly too small compared to the computer simulation. The agreement is nevertheless remarkable.

Next, we compare the approximation for the hole density with MC results. Here, we use Eq. (3.20) for the whole system since the approximations for both, upstream and downstream, interfaces result in a vanishingly small hole density except in the central region of the downstream interface. Invoking the normalization for the hole density (cf. Sec. 3.3), we plot the simulation data and the analytic approximation for  $\phi$  in Fig. 3.11. The parameter values are the same as in Fig. 3.10. A small quantitative discrepancy is observed at  $y = 0$ , i.e., the center of the downstream interface, whereas all other data points are remarkably well approximated by Eq. (3.20).

While for this system,  $L_x \times L_y = 16 \times 24$  and  $E = 0.8$ , the two interfaces are known to be well separated (which was our key assumption at the beginning of this Section), we state that the range of validity can be extended. Therefore we simply merge the tanh–functions, for instance by multiplication. This combined function captures the whole system and in comparison with simulation data, it gives remarkably good results even if the interfacial regions interfere; e.g. when  $L_y = 24$ ,  $E = 0.4$ , Fig. 3.9.

Given the results for the interfaces, we now turn to the order parameter  $Q_L$ . Here, we will see that the independent interface approximation provides us with a very sensitive test of the validity of our mean-field description.

Since the steady state exhibits complete order in one region of positive and another one of negative particles, the deviation of  $Q_L$  from unity originates near the interfaces. We can compute the contribution to  $Q_L$  for each interface separately, using Eq. (3.1). The wider (upstream) interface reduces  $Q_L$  by  $4/(\mathcal{E}L_y)$ , while the narrower downstream interface lowers it by  $2/(\mathcal{E}L_y)$ , resulting in a net  $Q_L = 1 - 6/(\mathcal{E}L_y)$ , in agreement with our earlier result, Eq. (3.12). For further reference, we summarize these two equations for the order parameter contribution  $Q_{L,i}$  of each interface:

$$Q_{L,i} = 1 - \frac{2\lambda_i}{\mathcal{E}L_y}; \quad (3.21)$$

where  $\lambda_d = 1$  for the downstream ( $i = d$ ) or  $\lambda_u = 2$  for the upstream ( $i = u$ ) interface.

Next, we aim to compare simulation data and the analytic approximations of  $Q_L$  separately for each interface. Therefore, we investigate systems with constant

$E L_y = 24$ . Note that the microscopic  $E$  appears here, for reasons that will become apparent shortly. Clearly, the interfaces are well separated from one another, cf. Fig. 3.7 or Fig. 3.9, so we can safely assume that they are independent. Varying the system size  $L_y$  from 12 to 48, the electric field covers the range between 0.5 and 2.0. 100 single runs of each system, with  $L_x = 24$ , are performed. The order parameter is then measured separately for each interface. To be precise, the order parameter contribution of the downstream interface,  $Q_{L,d}$ , is measured in the third of the system centered around the maximum hole density while the order parameter contribution of the upstream interface,  $Q_{L,u}$ , is determined in the remaining two thirds of the system. This reflects the proportion by which each interface reduces  $Q_L$  from unity. Of course, we round  $L_y/3$  and  $2L_y/3$  to the nearest integer.

Inserting our MC data for the two order parameter contributions,  $Q_{LMC,i}$ , into the analytic form for  $Q_{L,i}$ , Eq. (3.21), we can extract *estimates* for the effective drive and compare it to the *known* theoretical value of the mean-field  $\mathcal{E}$ . The latter is related to the microscopic  $E$ , at which the data were taken, through Eq. (2.12). Since this is performed separately at the two interfaces, we arrive at two estimates,  $E_{MC,i}$ , calculated via

$$E_{MC,i} = \frac{-2\lambda_i}{(Q_{LMC,i} - 1)L_i}. \quad (3.22)$$

Once again,  $\lambda_i = 1, 2$  for  $i = d, u$ , and  $L_i$  denotes the appropriate fraction of  $L_y$ :  $L_i = \lambda_i L_y/3$ . Thus,  $E_{MC,i}$  is the *effective* drive extracted from the measured order parameter  $Q_{LMC,i}$ . If our mean-field description holds well, we should observe good agreement of  $E_{MC,i}$  and  $\mathcal{E}$ . This expectation is tested in the upper two curves of Fig. 3.12, where we plot  $E_{MC,d,u}/\mathcal{E}$  vs.  $E$ , using Eq. (2.12) to find the appropriate values for  $\mathcal{E}$ . Two points are clearly observed. First, the data for the upstream interface lie slightly but systematically *above* those for the downstream interface: by about 0.03 on average. This is not inconsistent with Fig. 3.10: it appears that the downstream interface is better approximated by our analytic calculations than the upstream one. Second, and more surprisingly, the discrepancy between analytic and MC results *grows* with  $E$ : While it is about 6% for small values of  $E$ , it increases to 37% for the largest! Clearly, this forces us to take a closer look at these deviations. It is apparent that, in contrast to  $\mathcal{E}$ ,  $E_{MC}$  does not saturate, reminiscent of the microscopic  $E$ . We are therefore prompted to compare  $E_{MC}$  with the latter. Intriguingly, the ratio  $E_{MC,i}/E$ , plotted in two of the lower curves of Fig. 3.12, is nearly constant, even while  $E_{MC,i}/\mathcal{E}$  increases significantly! We have to conclude that Eq. (3.22) does not extract an *effective*  $\mathcal{E}$ , but instead the microscopic field  $E$  directly! Moreover, the systematic deviations observed for the upstream interface disappear here and the value of  $E_{MC,u}/E$  remains nearly constant at +4%.

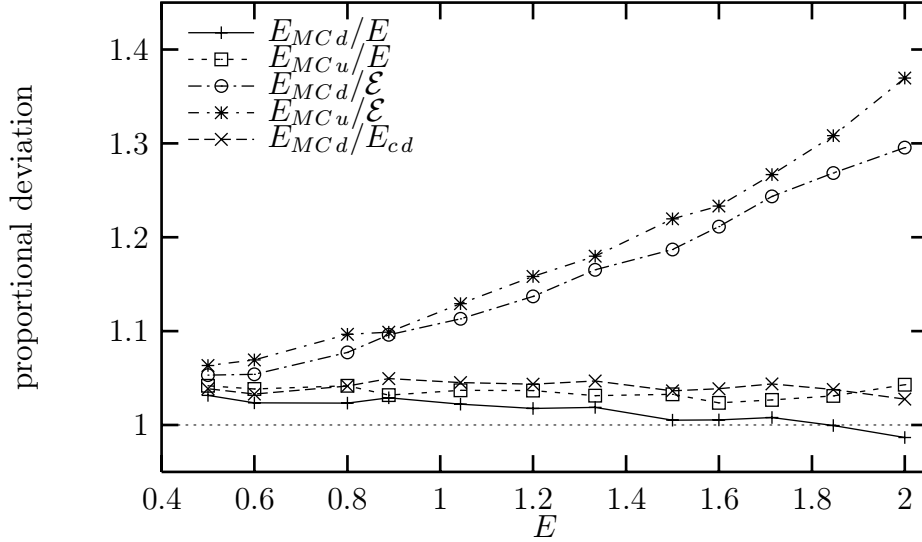


Figure 3.12: Comparison of  $\mathcal{E}$  and  $E$  obtained from simulations and analytic approximations for the distinct interfaces. See text for details. Systems with constant  $E L_y = 24$  and  $L_x = 24$  are used. The data are averaged over 100 runs.

A more careful look reveals that  $E_{MC,d}/E$  is still dependent, if rather weakly, on the electric field. With increasing field the ratio  $E_{MC,d}/E$  decreases, from about +3% for  $E = 0.5$  to  $-1\%$  for  $E = 2.0$ . The reason lies in the approximation used to obtain Eq. (3.19) from Eq. (3.18). To visualize the difference of these two interface approximations, we calculate the order parameter using Eq. (3.18):  $Q_{L,d} = \int dy [\sinh(Ey)/(\cosh(Ey) + 1/(2c))]^2$ . Substituting this order parameter in Eq. 3.22, we compute a corrected  $E_{cd}$  which takes into account the ( $E$ -dependent) coefficient  $c$  (Eq. 3.17). As a result, the  $E$ -dependence disappears in the ratio  $E_{MC,d}/E_{cd}$ , as shown in Fig. 3.12. There, the curve  $E_{MC,d}/E_{cd}$  remains nearly constant at +3%. Thus, the downstream interface is captured slightly better by its approximation than the upstream interface.

These results suggest two conclusions. First, it appears that mean-field theory overestimates the interfacial widths since the inequality  $E_{MC,i}/\mathcal{E} > 1$  follows easily from such an assumption. This is not surprising: the mean-field equations have been derived under the assumption of relatively slowly varying profiles, so that discrete MC data could be represented by continuous functions and second derivatives neglected. Thus, our equations can only be expected to describe profiles whose interfacial widths span (at least) a few lattice spacings. In contrast, the measured

profiles for, e.g.,  $E = 2.0$ , jump from 0 to almost 1 over a single lattice spacing, as we will see below. Second, and more disturbingly, we conclude that the electric field  $E$  controls the interface characteristics, rather than the effective drive  $\mathcal{E}$ . This should have a deep impact on our preceding work. Namely, in all equations, we should replace  $\mathcal{E}$  by  $E$ ; in addition,  $E$  should be used in the preceding scaling plots. Of course, this immediately raises the obvious question: How could we have observed such perfect agreement of MC data and analytic predictions, even though  $\mathcal{E}$ , or the related  $\epsilon$ , were used as scaling variables?

Clearly, we should expect disagreements only if  $E$  and  $\mathcal{E}$  differ appreciably, i.e., for  $E \gtrsim 1.0$ . In contrast,  $E = 0.8$  which translates into  $\mathcal{E} = 0.76$  should still give reasonable agreement with mean-field theory. This is especially the case for, e.g., the downstream interface in Fig. 3.10 where the difference between  $E = 0.8$  and  $\mathcal{E} = 0.76$  is even smaller since it is parsed through the tanh-function of the interface approximation, Eqs. (3.19).

Scanning through the remainder of our data, we see that  $E$ 's above 0.8 appear only in Figs. 3.3, 3.8 and 3.9. In Fig. 3.3, in particular, it is possible that the observed discrepancies between the data and the analytic curves might be reduced by using  $E$ , rather than  $\mathcal{E}$  in generating the latter. This calls for further investigation. In Figs. 3.8 and 3.9 it is surprising, at first, that the data for  $E = 1.0$  and 1.2 show little, if any, deviations from scaling. However, another much more subtle effect also plays a role in masking the errors arising through  $\mathcal{E}$ . This effect originates in the *shifts* that must be performed when measuring hole or charge density profiles.

To expose this effect, we take a closer look at charge density profiles  $\psi(y)$  of systems with large field, namely  $E = 2.0$  resulting in  $\mathcal{E} = 1.52$ . Here, the difference between  $E$  and  $\mathcal{E}$  is significant. A plot of the downstream interfacial region is given in Fig. 3.13. The different data points refer, first, to different system sizes and second, to different methods of locating the interface which will be described in the following.

The data “ $L_y = 8$ , shifted” and “non-shifted” (cf. the label inside Fig. 3.13) are obtained for a system with  $L_x = 32$  and  $L_y = 8$ . In addition, *brickwall* boundary conditions are implemented, and the simulations start from a completely *ordered* configuration: half of the system is occupied by positive particles, and the other half by negative ones, generating a sharp interface in the center. We now choose our  $y$ -axis such that  $y = 0$  marks the position of this interface, and note that it forms “between” two lattice rows. The hole is now placed into one of the adjacent lattice rows. For simplicity, we choose the same lattice row (at  $y = +0.5$ ) in all

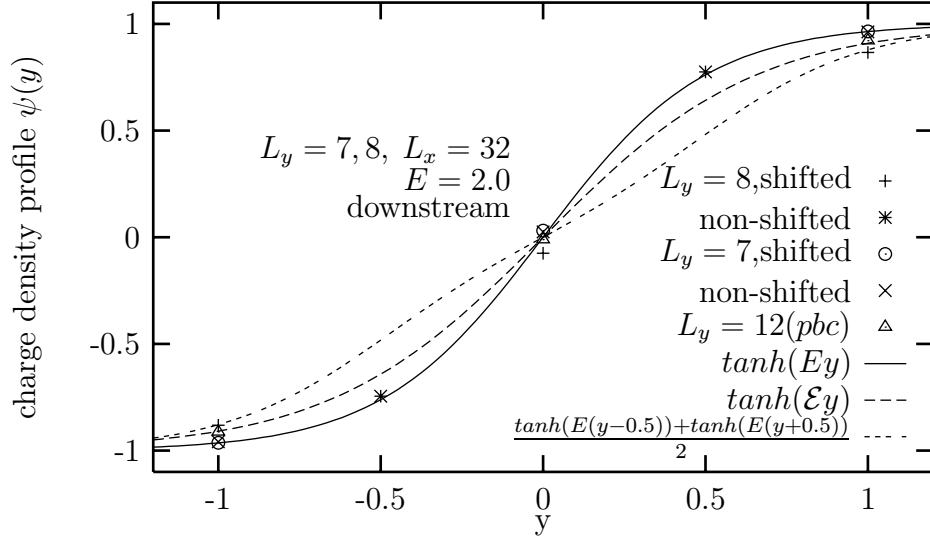


Figure 3.13: Charge density profile  $\psi(y)$  for the downstream interface with electric field  $E = 2.0$ . Different approximations and MC data are plotted (cf. text).

runs; however, this is not important since we are focusing on steady-state profiles only.

After the run is started, the hole “roughens” this interface, and soon the equilibrated downstream interface forms. The advantage of this procedure; namely, choosing brickwall boundary conditions and starting with an ordered initial configuration, is that we know the *exact* location of the downstream interface in all simulation runs, since it remains at  $y = 0$ . Thus, in order to average the data, a *shift* of the charge density profiles such that the hole density maxima coincide is not really necessary (cf. Section 2.2). Therefore, the unshifted data are displayed in Fig. 3.13. However, for comparison, we also plot the shifted data. Since the downstream interface sits “between” lattice rows, the maximum hole density is equally likely to be found at  $y = +0.5$  and  $y = -0.5$ . Thus, the shifted data of Fig. 3.13 consist of an average built from roughly equal numbers of profiles shifted by  $+1/2$  and  $-1/2$  lattice sites.

Further, we present the data for a system with  $L_y = 7$ , again using brickwall boundary conditions. Note that the completely ordered initial configuration now displays one lattice row which contains both positive and negative particles as well as the vacancy. Clearly, the location of the downstream interface, again placed

at  $y = 0$ , will now coincide with this lattice row. Again, a shift of the data is not really necessary, but we also compute the shifted data for comparison. In this case, however, the “non-shifted” and “shifted” data collapse, since the hole density maximum remains connected to a specific (i.e.,  $y = 0$ ) lattice row.

Last, data for a system with periodic boundary condition and random initial configuration is added to the plot. Here, we use  $L_y = 12$ ,  $L_x = 32$  and, again,  $E = 2.0$ .

Finally, three theoretical curves are shown in Fig. 3.13. First, we note that the unshifted data for the  $L_y = 8$  system as well as both, shifted and unshifted, data for the  $L_y = 7$  system are well described by a  $\tanh(Ey)$  profile. The mean-field  $\tanh(\mathcal{E}y)$  profile of Eq. (3.19) is also shown but is too wide to reproduce the data well, consistent with our observation that interfaces are better described by the microscopic  $E$  for large driving fields. It is also perfectly obvious that the mean-field profile overestimates the interfacial width, and hence predicts order parameter values that are too small.

It is interesting, however, that neither curve fits the *shifted* data for the  $L_y = 8$  system. Here, the averaging procedure distorts the actual charge density profile. Theoretically, we can imitate this effect by comparing the data with the curve  $[\tanh(E(y - 0.5)) + \tanh(E(y + 0.5))]/2$ , which indeed generates a good fit shown in Fig. 3.13.

The two “brickwall” systems discussed so far can be considered as extreme cases, compared to systems with periodic boundary conditions and random initial configuration: for the latter, the interface can form at arbitrary locations within the lattice, and hole density profiles may require any shift between 0 and 1, modulo multiples of the lattice spacing. Hence, the profiles of PBC systems lie *between* the borderline cases as illustrated by the “ $L_y = 12$  (pbc)” data shown in Fig. 3.13. Even though these data are well fitted by the  $\tanh(\mathcal{E}y)$ -profile, there is no systematic reason for this agreement. In particular,  $\tanh(\mathcal{E}y)$  will fall *outside* the other two theoretical profiles, once  $E \gtrsim 3.0$ . Returning to Figs. 3.8 and 3.9, we note that these show a system with PBC, so some distortion of the profiles, due to shifting, has taken place. However, for the  $E$ ’s shown there, the effect is even smaller than in Fig. 3.13 and unobservable on the scale of the plot.

In contrast to the profiles, the order parameter  $Q_L$  is insensitive to shifts, by virtue of its definition (2.7). It is therefore interesting to investigate an alternate order parameter which is constructed directly from the averaged charge density

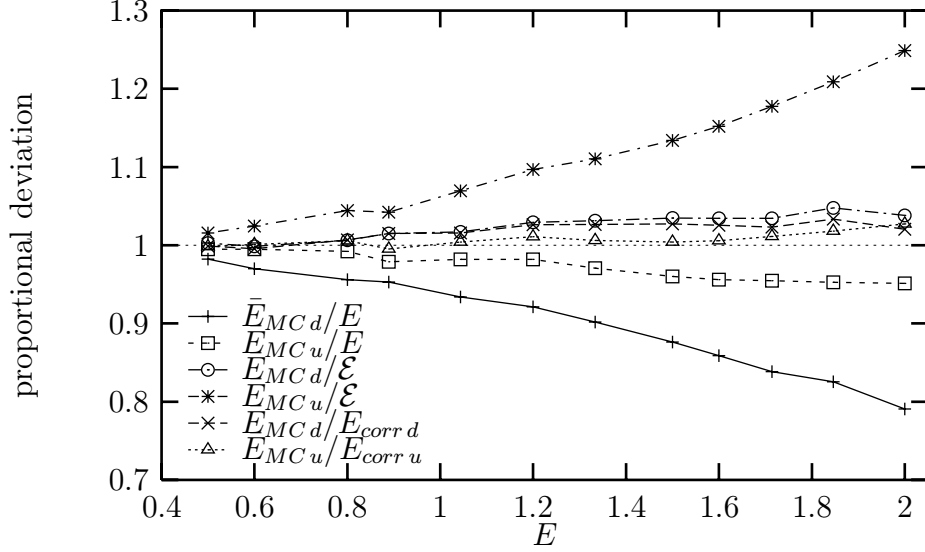


Figure 3.14: Similar to Fig. 3.12 except that  $\bar{Q}_{L,d,u}$  is used in order to calculate  $\bar{E}_{MC,d,u}$ , see text.

profile:

$$\bar{Q}_L = \frac{1}{L_y} \sum_y \langle \psi(y) \rangle^2 \quad (3.23)$$

Clearly, this quantity should carry information about the shifting procedure by which the averaged profiles are obtained (cf. Section 2.2). Moreover,  $\bar{Q}_L$  is designed to mirror the mean-field order parameter very closely.

Once again, we introduce the order parameter contributions  $\bar{Q}_{LMC,d}$  and  $\bar{Q}_{LMC,u}$  of each interface separately, and define  $\bar{E}_{LMC,i} = -2\lambda_i / [(\bar{Q}_{LMC,i} - 1) L_i]$ , with  $i = u, d$  depending on whether we focus on the upstream or downstream interface. Using the systems of Fig. 3.12, we plot the ratios  $\bar{E}_{MC,i}/E$  and  $\bar{E}_{MC,i}/\mathcal{E}$  vs  $E$  in Fig. 3.14. Focusing on the downstream interface, we observe that the ratio  $\bar{E}_{MC,d}/E$  decays rapidly with increasing field  $E$ : while it is 0.98 for  $E = 0.5$  it is about 0.79 for the largest investigated  $E = 2.0$ . In contrast, the ratio  $\bar{E}_{MC,d}/\mathcal{E}$  remains close to 1 over the whole range, never deviating more than +5%. These results are consistent with Fig. 3.13, where we observed good agreement between the theoretical  $\tanh(\mathcal{E}y)$  profile and the data for the downstream interface in a system with  $L_y = 12$  and periodic boundary conditions. In contrast, for the upstream interface,  $\bar{E}_{MC,u}/E$  provides better results than  $\bar{E}_{MC,d}/\mathcal{E}$ . While the deviations from unity for the small-

est fields are small in both cases ( $\leq \pm 3\%$ ), they increase up to  $-5\%$  for  $\bar{E}_{MC,d}/E$  and  $+25\%$  for  $\bar{E}_{MC,d}/\mathcal{E}$ .

In analogy to the discussion of Fig. 3.13, we can specify the error entering through the averaging process. There, we presented the borderline cases for the downstream interface, namely  $\tanh(Ey)$  and  $\frac{1}{2} [\tanh(E(y - 0.5)) + \tanh(E(y + 0.5))]$ . Similarly, we may assume that the corresponding borderline cases for the *upstream* interface are given by the same functions but with  $E$  replaced by  $E/2$ . Since both border line cases (and any in between) occur with the same probability, the actual charge density profile near each of the interfaces might be well captured by the arithmetic average:

$$\bar{\psi}(y) = \frac{1}{4} \{2 \tanh(Ey/\lambda_i) + \tanh(E(y + 0.5)/\lambda_i) + \tanh(E(y - 0.5)/\lambda_i)\} \quad (3.24)$$

where  $\lambda_d = 1$  and  $\lambda_u = 2$ , depending on whether we focus on the up- or downstream interface. Using  $\bar{\psi}$ , we can first calculate  $\bar{Q}_{L,i}$  from Eq. (3.23) and hence a corrected electric field  $\bar{E}_{corr,i}$  via Eq. (3.22). The corresponding data points  $\bar{E}_{MC,i}/\bar{E}_{corr,i}$  are also plotted in Fig. 3.14. For both interfaces, the deviations from unity are now quite small, remaining below 3%. Thus, the corrected drive provides a better fit to  $\bar{E}_{MC,i}$  than either  $E$  or  $\mathcal{E}$ . Once more we stress that, even though the data for  $\bar{E}_{MC,d}/\mathcal{E}$  and  $\bar{E}_{MC,d}/\bar{E}_{corr,d}$  lie closely together, this appears to be purely accidental. Finally, we comment on the relation of  $\bar{E}_{MC,d}/E$  and  $\bar{E}_{MC,u}/E$ . Recalling that the upstream interface is twice as wide as the downstream interface, the location of its center can be determined twice as precisely on the scale of the lattice spacing. Thus, the upstream contribution to the order parameter is known more precisely, giving us a better estimate of  $\bar{E}_{MC,u}$  compared to  $\bar{E}_{MC,d}$ , as borne out by Fig. 3.14. Moreover, we should expect that the error associated with the upstream interface at a given  $E$  should be comparable to the error in the downstream interface at  $E/2$  which is also confirmed by Fig. 3.14.

Reconsidering Fig. 3.12, we observe that  $\bar{E}_{MC,i}$  is always smaller than  $E_{MC,i}$ . This is easily understood as follows. Due to the shifting procedure, the *average* charge density profile is wider than the profiles of individual configurations. Thus, the order parameter  $\bar{Q}_L$  is reduced compared to  $Q_L$  since the latter is insensitive to shifts. As a consequence,  $E_{MC,i}$  is always the upper limit of  $\bar{E}_{MC,i}$ .

To summarize, all three preceding figures lead to the same conclusions, namely, that not the effective drive but rather the microscopic electric field should be used in the interface approximations, Eqs. (3.19) and (3.14). Thus, we discover an intriguing discrepancy between the analytical approach and the MC data. Given our discussion of the figures, it is apparent that the discreteness of the lattice plays a crucial role

once the width of either interface becomes comparable to the lattice spacing. Clearly, this is most pronounced at large fields since these generate very narrow interfacial regions (e.g. only about twice the lattice spacing, for the downstream interface at  $E = 2.0$ ). Then, the lattice sets a scale which is far too coarse for a precise determination of the maximum hole density. In contrast, this error is negligible for small  $E$ -fields, where the interfacial regions are much wider than a few lattice spacings. Moreover, as we pointed out earlier, we expect mean-field theory to break down when the profiles become too steep. It is therefore *very* surprising, that the *form* of our equations, (2.15) and (2.16), still appears to hold, provided we replace the effective drive  $\mathcal{E}$  by the microscopic field  $E$ . This purely phenomenological observation is not very well understood at this stage.

# Chapter 4

## Conclusions

### 4.1 Summary

In this work, we focused on the scaling behavior of ordered steady states in a simple lattice system. Therefore, we considered a two dimensional lattice  $L_x \times L_y$  with periodic boundary conditions filled by a nearly equal number of two species of particles such that only one site remains empty (the hole). The particles are referred to as plus and minus particles. They are biased to travel in opposite directions by an external field. Jumps against the field are suppressed exponentially. In analogy to the labelling of the particles, we refer to the field as electric field. The particles interact only through an excluded volume constraint. Moreover, in order to focus on the simplest case, particle-particle exchanges (i.e., a positive and a negative particle exchanging positions) are not allowed. Thus, the hole is the only mobile “particle” in the system.

With the help of Monte Carlo simulations, we established a simple scenario of the evolution leading to the steady state. Starting from a configuration in which particles are initially randomly distributed over the lattice, phase segregation occurs if  $EL_y$ , i.e., the product of drive and system size along the field direction), is sufficiently large. Then, a charge segregated strip, oriented transverse to the field, begins to form around the hole. As (MC) time progresses, the strip grows very slowly until it finally fills the whole system. In the steady state, half of the system is filled mostly by positive particles with the negative particles occupying the other half. The two oppositely charged regions are separated by two interfaces with distinct characteristics: One interface, referred to as “downstream”, attracts the

hole, the other (upstream) repels it strongly. This asymmetry finds its origin in the charge separation induced by the external field: while the hole moves rapidly *along* the field in the negative region, its preferred direction is reversed in the positive region.

Much research on our model was carried out in earlier studies [17], [20]. To quantify simulation data, an order parameter was introduced which essentially counts the ordered rows transverse to the field. On the analytic side, a mean-field theory was developed in which the drive appeared through the effective parameter  $\mathcal{E} \equiv 2 \tanh(E/2)$ . In our work, a calculation of  $Q_L$  in the frame of mean-field theory resulted in  $Q_L \simeq 1 - 6/(m\epsilon)$ , for large  $\epsilon \equiv \mathcal{E}L_y$ . For our case, which focuses on a single hole ( $m \equiv 1$ ), phase separation requires  $\epsilon \geq 2\pi$ . At first sight, our Monte Carlo simulations for a system with a single hole appear to confirm that the order parameter depends entirely on  $\epsilon$ . However, a more careful analysis reveals that  $E$ , rather than  $\mathcal{E}$ , determines the behavior of the model. We first summarize how we arrived at this result.

Some of our more detailed studies concentrated on the hole and charge density profiles along the field direction in the steady state. Confirming theoretical predictions [20], Monte Carlo data of both densities satisfy scaling in  $\epsilon$  and  $z = y/L_y$ , at least for sufficiently small ( $E \lesssim 0.8$ ) values of the drive. We note that, with regard to the steady state, the transverse system size  $L_x$  appears to affect finite-size corrections only. Going into more detail, we investigated the longitudinal size and field dependence of the density profiles. We observed, in particular, that the width and slope of the interfacial regions are independent of  $L_y$ , provided that they do not overlap. Under these conditions, the two interfaces are separated by two fully charge-segregated regions, in which the charge density reaches its saturation value,  $\pm 1$ . The structure of the ordered inhomogeneous state is then reflected by the interfaces alone. Here, Monte Carlo data provided first information. Independent of  $L_y$ , the characteristics of the interfaces appear to scale with the effective drive  $\mathcal{E}$ . Turning again to mean-field theory, two independent approximations were developed for the interfaces (downstream and upstream), valid only in the region of each interface. Focusing first on the upstream interface, we note that the hole density is vanishingly small there. In mean-field theory, this is equivalent to taking the large  $\epsilon$  limit. Then, the charge density of the upstream interface is described by the simple equation  $\psi(y) = -\tanh(\mathcal{E}y/2)$ , Eq. (3.14). For the downstream interface, we solve the mean-field equations directly, under the assumption that both, charge and mass, currents vanish. With appropriate boundary conditions, this equilibrium-like approximation leads to the explicit forms of the profiles, Eqs. (3.19) and (3.20):  $\psi(y) = \tanh(\mathcal{E}y)$  and  $\phi(y) = 1/(2c \cosh(\mathcal{E}y))$ . Simulation data indicate excellent

agreement with these density profiles.

These results can be used to compute the order parameter  $Q_L$ . We recall that the system is fully ordered in the two regions between the interfaces. Moreover, for a perfectly ordered lattice, the order parameter would take its maximum value: unity (up to a trivial finite size effects for odd  $L_y$ ). Thus, any reduction of  $Q_L$  is due to the interfacial regions. These order parameter contributions can be determined separately for each interface, using both simulations and mean-field theory. Regarding the latter, the upstream interface reduces  $Q_L$  by  $4/(\mathcal{E}L_y)$  and the downstream by  $2/(\mathcal{E}L_y)$ , the total being in agreement with our former result  $Q_L = 1 - 6/(\mathcal{E}L_y)$ .

At this juncture, we observe the first serious discrepancies between MC data and mean-field theory predictions. Using data over a large range of fields, i.e.,  $0.5 \leq E \leq 2.0$ , systematic deviations are observed when attempting to fit the data to mean-field expressions, using the effective field  $\mathcal{E}$ . These deviations are most pronounced at large fields, i.e.,  $E \geq 1.2$ . Surprisingly, they are significantly reduced if we substitute the *real* microscopic field  $E$  for the effective  $\mathcal{E}$  in the (mean-field) interface approximations. On the one hand, we can easily trace the origin of this breakdown of mean-field theory to the fact that interfacial widths, at large fields, are comparable to just a few lattice spacings. Not surprisingly, the usual mean-field theory fails to capture such sharp profiles. On the other hand, it is not clear at this point why  $E$  appears to be the appropriate parameter in the mean-field equations, rather than  $\mathcal{E}$ . Our previous results did not expose this effect for two reasons: First, relatively small electric fields were chosen ( $E \leq 1.2$ ) such that the difference between  $\mathcal{E}$  and  $E$  remained below 10%. Second, the shifting process which is used to obtain averaged profiles widens the interfacial regions artificially, so that it is much more difficult to observe deviations from  $\mathcal{E}$ -scaling in profiles than in the order parameter  $Q_L$ . In fact, only a very careful analysis of a strongly driven ( $E = 2.0$ ) charge density profile, Fig. 3.13, was able to expose the subtle difference between mean-field theory and computer simulations.

## 4.2 Further Discussion

In the following, we list several remarks and comments arising from the study of our model system.

In Ref. [18], the authors discovered that systems with large aspect ratio  $L_x/L_y$  order not only into transverse strips but also, with significant probability, into *tilted*

strips (“barber poles”) with non-zero integer winding number. It is also easy to see that the mean field equations allow for these solutions. In contrast to our studies, however, the mass density was chosen to be much smaller ( $m = 0.5$  in [18]). This fact may explain why we never observed any tilted strips in this work even though our aspect ratios could be as large as  $L_x/L_y = 100/16$ . Nevertheless, some simulations with  $L_x/L_y > 5$  showed strips which were quite curved at early times and then straightened in a very slow process resulting in the steady-state configuration. This may indicate that systems near complete filling require much larger aspect ratios before tilted strips can occur with non-negligible probability. Further studies are clearly needed.

Otherwise, the transverse system size  $L_x$  appears only in the constant  $c$  (cf. Eq. 3.17), which enters into the approximation for the density profiles of the downstream interfacial region. In contrast, the approximation for the upstream interface is completely independent of  $L_x$ . This distinction between the two interfaces can be intuitively understood as follows. Since the probability of finding the hole at a given position is non-negligible only in the downstream interfacial region, variations of the hole density should only affect this region.  $L_x$  then enters through the hole density via  $1 - m = 1/(L_x Ly)$ .

In the detailed analysis of the interfaces in the context of Fig. 3.12, we did not discuss possible origins of the *remaining* discrepancies between the MC data and mean-field theory. For both interfaces,  $E_{MC}$  still exceeds the microscopic  $E$  by about 3 – 4%. This appears to be a finite size effect: Using systems with a much larger transverse size  $L_x$ , the deviations decrease significantly [31]. Presumably, fluctuations in the central interfacial regions increase the order parameter, since they are summed up in  $Q_L$  (cf. Section 2.2). A larger  $L_x$  results in smaller fluctuations and, thus, in a more “accurate” order parameter as well as a more “accurate”  $E_{MC}$ . It is interesting that the interfaces appear to be very straight, as we already noted in our remark concerning the absence of barber poles.

For small electric fields ( $E \lesssim 0.8$ ), we found very good quantitative agreement between simulation data and mean-field theory. Referring to the preceding paragraph, this can be further improved by taking data at larger  $L_x$ . Hence, the approximations leading to our mean-field theory should be satisfied by the microscopic system for this range of  $E$ . First, we assumed that two-point correlations should be small, in order to write a closed equation for one-point functions (see Section 2.5). Indeed, we do not expect that these correlations have a significant influence with the choice of our parameters. The lowest order corrections to our mean field equation (given explicitly in [26]) are extremely small for our model system. Second, we neglected

higher than second derivatives when taking the continuum limits in Eqs. (2.13) and (2.14). Clearly, the latter requires that the profiles vary slowly on the scale of the lattice spacing. Considering the charge density profile at the downstream interface,  $\psi(y) \simeq \tanh(\mathcal{E}y)$ , and recalling that the lattice spacing was set to 1, we have to choose  $\mathcal{E} \lesssim 0.5$  in order to satisfy this requirement. Even though the quantitative agreement of data and mean-field theory deteriorates for higher fields, some of the key predictions of the theory are still observed, such as the phenomenon of charge segregation. Moreover, we showed in Section 3.5 that the quantitative success of our mean-field theory can be “extended” to larger fields by using the microscopic  $E$  in the place of the effective drive  $\mathcal{E}$ .

Recalling the equilibrium approximation for the downstream interfacial region, another point of view opens. We should be able to capture this part of the system with usual techniques of the equilibrium statistical mechanics. In principle, finding the Hamiltonian and calculating the partition function are the first steps leading to the charge and hole densities. However, there is an easier way to progress considering the Fermi-Dirac distribution. Note, that this distribution assumes a state is either occupied or vacant. Neglecting the hole in our system, this is translated into: a state is either occupied by a minus or plus particle. As a consequence, the energy term ( $\pm Ey$ ) in the Fermi-Dirac distribution suffers a doubling. In the final result (including a calculation of the chemical potential), the charge density profile is given by  $\tanh(Ey)$ . We observe the correct (with regard to the MC data) microscopic field appears in the tanh-function. However, the hole density has to be 0 since we simply neglected it here. A more extensive calculation may capture this lack, but is outside the scope here.

### 4.3 Outlook

Within the range of parameters investigated here, the steady-state characteristics of our model are quite well understood, in the frame of both MC simulations and mean-field theory. We captured the influence of all system parameters ( $L_x$ ,  $L_y$  and  $E$ ) on relevant quantities such as the order parameter and the hole and charge density profiles.

However, some questions about the divergence between mean-field theory and simulation data require further clarification. For instance, the mean-field theory breaks down quantitatively for the system, where as an equilibrium description (see last paragraph in the preceding section) presents excellent agreement with the MC

data, at least for the downstream interface. In order to understand this behavior, it would be interesting to set up a dynamic equation for the downstream interface in the frame of equilibrium statistical mechanics and compare it with the mean field equations here.

Beyond steady-state characteristics, the dynamics of the system also constitutes an intriguing problem. One would like to explore and understand the mechanisms underlying the ordering process and seek for possible scaling properties. Work on ordering phenomena in the single-vacancy case is in progress and will be published later [31].

Though our model is very simple, it provides basic information that is relevant to a large variety of related problems [1]. Here, we mention only one of many possible generalizations [28]: Particle–particle exchanges may be allowed in addition to particle-hole exchanges, occurring in general on a different time scale. While most of the phase diagram for this model is well established, questions about its behavior near complete filling remain open.

# Bibliography

- [1] B. SCHMITTMANN AND R.K.P. ZIA, *Phase Transition and Critical Phenomena Vol. 17*, eds. C. DOMB AND J.L. LEBOWITZ (Academic, New York, 1995).
- [2] S. KATZ, J.L. LEBOWITZ AND H. SPOHN, *Phys. Rev. B* 28, 1655 (1983) and *J. Stat. Phys.* 34, 497 (1984).
- [3] D. J. AMIT, *Fieldtheory, the Renormalization Group, and Critical Phenomena*, (World Scientific, Singapore, 1984); H.K. JANSSEN, *Z. Phys. B* , 23, 377 (1976); C. DEDOMINICS, *J. Phys.*, 37, C1-247 (1976).
- [4] H.K. JANSSEN AND B. SCHMITTMANN *Z. Phys. B* 64, 503 (1986); K.-T. LEUNG AND J.L. CARDY *Stat. Phys.* 44, 567 (1986).
- [5] B. SCHMITTMANN AND R.K.P. ZIA *Phys. Rev. Lett.* 66, 357 (1991).
- [6] M.Q. ZHANG, J.-S. WANG, J.L. LEBOWITZ AND J.L. VALLES *J. Stat. Phys.* 52, 1461, (1988); P.L. GARRIDO, J.L. LEBOWITZ, C. MAES AND H. SPOHN *Phys. Rev. A* 42, 1954 (1990); G. GRINSTEIN, D.H. LEE AND S. SACHDEV *Phys. Rev. Lett.* 64, 1927 (1990); R.K.P. ZIA, K. HWANG, B. SCHMITTMANN AND K.-T. LEUNG, *Physica A* 194, 183 (1993).
- [7] K.-T. LEUNG, K.K. MON, J.L. VALLES AND R.K.P. ZIA, *Phys. Rev. Lett.* 61, 1744 (1988); K.-T. LEUNG, K.K. MON, J.L. VALLES AND R.K.P. ZIA, *Phys. Rev. B* 39, 9312 (1989); J.L. VALLES, K.-T. LEUNG, R.K.P. ZIA, *J. Stat. Phys.* 56, 43 (1989); K.-T. LEUNG, R.K.P. ZIA, *J. Phys A* 24, 1399, (1991); K.-T. LEUNG, R.K.P. ZIA, *J. Phys A* 26, L737, (1993); F.J. ALEXANDER, C.A. LABERGE, J.L. LEBOWITZ AND R.K.P. ZIA, *J. Stat. Phys.* 82, 1133 (1996); M. ANDERSON, *Thesis VPI&SU* (1998).
- [8] K.-T. LEUNG, *Phys. Rev. Lett.* 66, 453, (1991); K.-T. LEUNG, *Int. J. Mod. Phys. C*3, 367, (1992); K.-T. LEUNG AND J.-S. WANG, *Los Alamos preprint cond-mat/9805285*, (1998).

- [9] e.g. S. CHANDRA, *Superionic Solids. Principles and Applications*, (North-Holland, Amsterdam, 1981).
- [10] M. AERTSENS AND J. NAUDTS, *J. Stat. Phys.*, 62, 609 (1990).
- [11] O. BIHAM, A.A. MIDDLETON AND D. LEVINE, *Phys. Rev.* A46, R6124 (1992); K-T. LEUNG, *Phys. Rev. Lett.* 73, 2386 (1994); J.M. MOLERA, F.C. MARTINEZ AND J.A. CUESTA, *Phys. Rev.* E51, 175 (1995).
- [12] M. RUBINSTEIN, *Phys. Rev. Lett.* 59, 1946 (1987); T.A.J. DUKE, *Phys. Rev. Lett.* 62, 2877 (1989); Y. SHNIDMAN, *Mathematical and Industrial Problems IV* ed. A. FRIEDMAN (Springer, Berlin, 1991); B. WIDOM, J.L. VIOVY AND A.D. DESFONTAINES, *J. Phys. I* (France) 1, 1759 (1991).
- [13] F.Y. WU, *Rev. Mod. Phys.* 54, 235 (1982).
- [14] J. ASHKIN AND E. TELLER, *Phys. Rev.* 64, 178 (1943).
- [15] M. BLUME, V.J. EMERY AND R.B. GRIFFITHS, *Phys. Rev.* A4, 1071 (1971).
- [16] W. SELKE, *Phase Transition and Critical Phenomena Vol. 15*, eds. C. DOMB AND J.L. LEBOWITZ (Academic, New York, 1993).
- [17] B. SCHMITTMANN, K. HWANG, R.K.P. ZIA, *Europhys. Lett.* 19, 19 (1992).
- [18] K.E. BASSLER, B. SCHMITTMANN AND R.K.P. ZIA, *Europhys. Lett.* 24, 115 (1993).
- [19] D.P. FOSTER AND C. GODRÈCHE, *J. Stat. Phys.* 76, 1129 (1994).
- [20] I. VILFAN, B. SCHMITTMANN AND R.K.P. ZIA, *Phys. Rev. Lett.* 73, 2071 (1994).
- [21] A.-L. BARABÁSI AND H.E. STANLEY, *Fractal Concepts in Surface Growth* (Cambridge University Press, 1995).
- [22] J.S. LANGER, *Solids Far From Equilibrium*, ed. C. GODRÈCHE, (Cambridge University Press, 1992); A. BRAY, *Adv. Phys.* 43, 357 (1994).
- [23] see, e.g., W.D. CALLISTER JR., *Materials Science and Engineering: An Introduction*, (Wiley, 1994); Z. TOROCZKAI, G. KORNISS, B. SCHMITTMANN AND R.K.P. ZIA, *Europhys. Lett.* 40, 281 (1997).
- [24] N. METROPOLIS, A.W. ROSENBLUTH, M.N. ROSENBLUTH, A.H. TELLER AND E. TELLER, *J. Chem. Phys.* 21, 1087 (1953).

- [25] see, e.g., K. BINDER, *Applications of the Monte Carlo Method in Statistical Physics*, (Springer–Verlag, Berlin, 1983).
- [26] K.–T. LEUNG AND R.K.P. ZIA, *Phys. Rev. E* 56, 308 (1997).
- [27] K.–T. LEUNG, *Phys. Rev. Lett.* 66, 453 (1991).
- [28] G. KORNISS, B. SCHMITTMANN AND R.K.P. ZIA, *J. Stat. Phys.* 86, 721 (1997); G. KORNISS, *PhD Thesis*, (Virginia Polytechnic Institute and State University, 1997).
- [29] *Numerical Recipes in C, The Art of Scientific Computation*, (Cambridge University Press, 1988–92).
- [30] Notation from M. ABRAMOWITZ AND I.A. STEGUN, *Handbook of Mathematical Functions*, (Dover, New York, 1970), Chap. 16 and 17.
- [31] M. THIES, *Diplomarbeit*, to be published (Technische Universität Braunschweig, 1998).

# Appendix A

## Source Codes

### A.1 Typical C Source Code for the Simulations

In this section, we list a printout of the Monte Carlo simulation program written in C. We omit a detailed explanation of the program, however, a comment on the heart of the program, the Metropolis algorithm, is in order. Thus, a comparison with the slightly different algorithm in the Sec. A.2 is possible.

The loop in the *main()* program counting the MCS calls in each step, i.e. an increment of MCS by 1, the function *simulation()* which decides of whether a particle-hole exchange takes place or not. The variables of the function *simulation(on,hx,hy,iseed)* are the occupation variable of the lattice site  $on(= n_{xy}^+ - n_{xy}^-)$  where  $(0 \leq x, y < L_{x,y}; x, y \text{ integer})$ , the position of the hole  $(hx, hy)$  and the seed for the random number generator. The loop in *simulation* selects in each step a hole of the system at random. Since our investigations focus on systems with only one hole (NH=1), this hole is always chosen ( $rh = 0$ ) and the loop is actually run through only once. Next, a random number  $rd$  is drawn out of  $\pm 1, \pm 3$  which fixes the direction in which the hole will attempt to move: A positive (negative) number points to the positive (negative) direction and one labels the x-axis, three the y-axis. Now, another random number  $(0 \leq p \leq 1)$  is drawn. The Metropolis rates, cf. Eq. (2.1), (here,  $\tau_s = LP = TP \equiv 1$ ) are used to check if the trial is successful. If the trial is successful, the particle exchange place with the hole and the program returns to the *main* function. Otherwise, the program returns to the *main* function without exchanging hole and particle.

```

/*****
* MC simulation : sim.c
*
* copyright Michael Thies 5/1997
*****/
#include <stdio.h>
#include <math.h>
#include <time.h>

#define E 0.8
#define LX 16
#define LY 24
#define NH 1
#define TP 1.0 /*transveral transition probability*/
#define LP 1.0
#define MAX 500
#define FILETIME "r241608t.dat"
#define FILEEND "r241608e.dat"
#define FILEOUT "r241608p.dat"
#define PARAPOS 1 /*parameter position of the changing number*/
#define CONFIG 1 /* 1 - random configuration
                2 - complete order
                beginning of the simulation */
/*****
* constants for random generator
*****/
#define IM1 2147483563
#define IM2 2147483399
#define AM (1.0/IM1)
#define IMM1 (IM1-1)
#define IA1 40014
#define IA2 40692
#define IQ1 53668
#define IQ2 52774
#define IR1 12211
#define IR2 3791
#define NTAB 32
#define NDIV (1+IMM1/NTAB)
#define EPS 1.2e-7
#define RNMIX (1.0-EPS)
/*****
void main()
{
    short int on[LX][LY];
    int hx[LX],hy[LY];
    int e,i,j,s,nos,jsam,center,shift;
    int wh[MAX][LY],w[LY];
    long it=100,ite=1,mcs,MCS,mcstep[MAX];
    long iseed=-time(NULL); /* sets the seed for random generator*/
    float av_pd[MAX][LY];
    float fati[MAX],av_Q[MAX],psi[MAX][LY],Q[MAX];
    void occupy_random();
    void functionpsi(),convert(),occupy_order(),watchhole();
    float orderparameterq(),simulation();
    char file[50]=FILETIME,file[50]=FILEEND,*f,*g;
    FILE *fpt, *fp, *fopen();

```



```

    }
    jsam+=1;
    fprintf(fp, "\n#mct    %ld", mcstep[j]);
    fprintf(fp, "\n#holedistribution\n");
    for (i=0; i<LY; i++)    fprintf(fp, "%d    ", wh[j][i]);
    fprintf(fp, "\n#psiprofile\n");
    for (i=0; i<LY; i++)    fprintf(fp, "%f    ", psi[j][i]);
    if (mcstep[j]>70000){
        j+=8;
    }
    else j+=4;
}
}
for (i=0; i<e; i++){
    av_Q[i]/=nos;
    for (j=0; j<LY; j++) av_pd[i][j] /= nos;
    for (j=0; j<LY; j++) fati[i] += (av_pd[i][j] * av_pd[i][j]) ;
}

fpt = fopen(filet, "w");                                /*file which save
                                                         time evolution of Q*/
for (i=0; i<e; i++) fprintf(fpt, "%12ld%c%f%c%f%c%f\n",
    mcstep[i], 9, fati[i], 9, av_Q[i], 9, (av_Q[i]/(float)(LY)+1.0/(float)(LX))    );
fprintf(fpt, "\n#%s%d\n#%s%d\n#%s%d\n#%s%ld", "LX= ", LX, "LY= "
    , LY, "NH= ", NH, "MCS= ", MCS);
fprintf(fpt, "\n#nos=%d \n#E= %f \n#TP= %f \n#LP= %f", nos, E, TP, LP);
fprintf(fpt, "\n#mcs    barQ    (Q-1/LX)*m*LY    Q1*m\n#data \n");

fclose(fpt);
fprintf(fp, "#EOF");
rewind(fp);
fprintf(fp, "#it= %ld", it);
fprintf(fp, "\n#jm= %ld", jsam);
fclose(fp);
convert(file);
}
/*****start the subroutines of main program asim.c *****/
void convert(file) /*subroutine to extract profiles from the saved
                  data; can be handled as a separate program with
                  preamble of main program*/

char file[];
{
    int i, j, d, h, k, jm, shift, center, nos;
    int av_h[MAX][LY], holes[MAX][LY], pdhy[MAX][LY];
    long int mct[MAX];
    float av_psi[MAX][LY], profile[MAX][LY];
    float p;
    int maxholedensity();
    int sumhole();
    char filep[50]=FILEOUT, *f, *g;
    char str[100];
    FILE *fp, *fpp, *fopen();

    fp = fopen(file, "r");
    fpp = fopen(filep, "w");

    while (fscanf(fp, "%s", str) && strcmp("#nos=", str));
    fscanf(fp, "%d", &nos);
    rewind(fp);

```

```

while (fscanf(fp,"%s",str) && strcmp("#jm=",str));
fscanf(fp,"%d",&jm);
rewind(fp);
for (j=0; j<MAX; j++){
    for (i=0; i<LY; i++) {
        av_psi[j][i] = 0;
        av_h[j][i]= 0;
    }
}
for (i=0; i<nos; i++){
    for (k=0; k<jm;k++){
        while (fscanf(fp,"%s",str) && strcmp("#mct",str));
        fscanf(fp,"%ld",&mct[k]);
        while (fscanf(fp,"%s",str) && strcmp("#holedistribution",str));
        for (j=0; j<LY; j++){
            fscanf(fp,"%d",&d);
            holes[k][j]=d;
        }
        center = maxholedensity(holes,k);
        shift = (LY/2) - center;
        for (j=0; j<LY; j++) pdhy[k][j]=holes[k][ (LY+j-shift)%LY];
        while (fscanf(fp,"%s",str) && strcmp("#psiprofile",str));
        for (j=0; j<LY; j++){
            fscanf(fp,"%f",&p);
            profile[k][ (LY+j+shift)%LY]=p;
        }
        for (j=0; j<LY; j++) {
            av_psi[k][j]+=profile[k][j];
            av_h[k][j]+=pdhy[k][j];
        }
    }
}
fpp = fopen(filep,"w");
for (h=0; h<jm; h++){
    fprintf(fpp,"#mct:%ld\n",mct[h]);
    for (i=0; i<LY; i++){
        fprintf(fpp,"%d      %f      %f      %f\n",i-LY/2,
            ((float)i-LY/2.0)/(float)(LY),
            (av_psi[h][i]/nos),
            (((float) av_h[h][i])/((float) sumhole(av_h,h))));
    }
}
fprintf(fpp,"\n\n");
rewind(fp);

while (fscanf(fp,"%s",str) && strcmp("#LX=",str));
i=0;
do {
    fprintf(fpp,"%s",str);
    i+=1;
    if ((i % 2)== 0) fprintf(fpp,"\n");
} while (fscanf(fp,"%s",str) && strcmp("#samplenumber=",str));
for (k=0; k<jm; k++) fprintf(fpp,"\n#mctimes %ld",mct[k]);

fclose(fpp);
fclose(fp);
}
/*****
int sumhole(av_h,j)
int j;

```

```

int av_h[MAX][LY];
{
    int i,sum=0;

    for (i=1; i<LY; i++) sum+=av_h[j][i];
    return (sum);
}
/*****/
int maxholedensity(pdhy,j)
int pdhy[MAX][LY];
int j;
{
    int i,max,center=0;

    max = pdhy[j][0];
    for (i=1; i<LY; i++)
        if (max <= pdhy[j][i] ){
            center = i;
            max = pdhy[j][i];
        }
    return (center);
}
/*****/
void watchhole(w,hy)
int w[];
int hy[];
{
    int i;
    for (i=0; i<NH; i++) w[hy[i]]+=1;
}
/*****/
void occupy_order(on,hx,hy)
short int on[LX][LY];
int hx[NH],hy[NH];
{
    int h,x,y,m1,m2,i;
    void prn_config_screen();

    for (y=0; y < LY/2; y++)
        for (x=0; x<LX; x++) on[x][y] = -1;
    for (y=LY/2; y<LY; y++)
        for (x=0; x<LX; x++) on[x][y] = 1;
    if ((LY/2) < ((LY+1)/2)){
        for (x=0; x < (LX+1)/2; x++) on[x][LY/2] = -1;
        if (NH>LX) {
            printf("\n%s\n%s", "The amount of holes must be fewer than LX",
                "error--error--error");
            return;
        }
        else m1=(LX-NH)/2;
        m2 = (LY)/2;
        for (x=m1; x<(m1+NH); x++){
            on[x][m2]=0;
            hx[x-m1]=x;
            hy[x-m1]=m2;
        }
    }
    else{
        h=(int) ((NH+1)/2);
        m1=(int) ((LX-h)/2);
    }
}

```

```

    m2 =(LY-1)/2;
    for (x=m1; x<(m1+h); x++){
        on[x][m2]=0;
        hx[x-m1]=x;
        hy[x-m1]=m2;
    }
    i=(int) (NH-h);
    m2 =(LY)/2;
    for (x=m1; x<(m1+i); x++){
        on[x][m2]=0;
        hx[x+h-m1]=x;
        hy[x+h-m1]=m2;
    }
}
}
}
/*****/
void occupy_random(on,hx,hy,iseed)
short int on[LX][LY];
int hx[NH],hy[NH];
long *iseed;
{
    int m1,m2,pm,x,y,i,rx,ry;
    float ran2(long *iseed);

    for (x=0; x<LX; x++)                /*occupy all with + particles*/
        for (y=0; y<LY; y++)
            on[x][y]=1;

    if (NH>LX) {                          /*implent holes in the middle */
        printf("\n%s\n%s", "The amount of holes must be fewer than LX",
            "error--error--error");
        return;
    }
    else m1=(LX-NH)/2;
    m2 = LY/2;
    for (x=m1; x<(m1+NH); x++){
        on[x][m2]=0;
        hx[x-m1]=x;
        hy[x-m1]=m2;
    }

    pm = ((LX * LY) - NH )/2;              /*placing the - particles */
    i=0;                                   /*# of - is equal to # of + or*/
    while (i<pm){                          /*only one lower than +(#odd) */
        rx=(int) (LX * ran2(iseed)) ;
        ry=(int) (LY * ran2(iseed)) ;
        if ((on[rx][ry] != -1) && (on[rx][ry] != 0)){
            on[rx][ry]=-1;
            i++;
        }
    }
}
}
/*****/
float simulation(on,hx,hy,iseed)
short int on[LX][LY];
int hx[],hy[];
long *iseed;

{
    int i,rh,rd,nn;

```

```

float p,ran2(long *iseed);
double exp();

for (i=0; i<NH; i++){
  if (NH==1) rh=0;
  else rh=(int) ( NH * ran2(iseed));          /*choose hole      */
  rd=(int) ( 4.0 * ran2(iseed));             /*choose direction */
  rd=(rd - 1.5)*2;                           /*implies          */
                                              /*period.boundaries*/
                                              /* 3 y-axis       */
                                              /* 1 x-axis       */

  if (rd == -3) nn=on[hx[rh]] [(LY+hy[rh]-1)%LY];
  if (rd == -1) nn=on[(LX+hx[rh]-1)%LX] [hy[rh]];
  if (rd == 1) nn=on[(hx[rh]+1)%LX] [hy[rh]];
  if (rd == 3) nn=on[hx[rh]] [(hy[rh]+1)%LY];

  p=ran2(iseed);

  if ((rd == 1) && (p > TP)) continue;
  if ((rd == -1) && (p > TP)) continue;
  if ((rd == 3) && (nn == 1) && (p > (LP * exp(-E)))) continue;
  if ((rd == 3) && (nn == -1) && (p > LP)) continue;
  if ((rd == -3) && (nn == 1) && (p > LP)) continue;
  if ((rd == -3) && (nn == -1) && (p > (LP * exp(-E)))) continue;
  if (nn == 0) continue;

  on[hx[rh]] [hy[rh]]=nn;

  if (rd == -3) hy[rh]=((LY+hy[rh]-1)%LY);
  if (rd == -1) hx[rh]=((LX+hx[rh]-1)%LX);
  if (rd == 1) hx[rh]=((hx[rh]+1)%LX);
  if (rd == 3) hy[rh]=((hy[rh]+1)%LY);
  on[hx[rh]] [hy[rh]]=0;
}
}
/*****/
void functionpsi(on,psi,e)
short int on[LX] [LY];
float psi[] [LY];
int e;
{
  int x,y,a;

  for (y=0; y<LY; y++){
    a=0;
    for (x=0; x<LX; x++) a += on[x] [y];
    psi[e] [y]= ((float)(a) / (float)(LX));
  }
  return;
}
/*****/
float orderparameterq(psi,j)
int j;
float psi[] [LY];
{
  int y;
  float q=0.0;
  float m;

  /*m= (float) (LX*LY-NH)/(float) (LX*LY);*/

```

```

m=1.0;

for (y=0; y<LY; y++) q = q + (psi[j][y]) * (psi[j][y]);
return ((q/m)-1.0/LX*LY);
}
/*****random generator*****/
float ran2(long *idum)
/*Long period (> 2 10^18 ) random number generator of L'Ecuyer with
Bays-Durham shuffle and added safeguards. Returns a uniform random
deviate between 0.0 and 1.0 (exclusive of the endpoint values).
Call with idum a negative integer to initialize; thereafter, do not
alter idum between successive deviates in a sequence. RNMX should
approximate the largest floating value that is less than 1.*/
{
int j;
long k;
static long idum2=123456789;
static long iy=0;
static long iv[NTAB];
float temp;

if (*idum <= 0) { /* Initialize.*/
if (-(*idum) < 1) *idum=1; /* Be sure to prevent idum = 0*/
else *idum = -(*idum);
idum2=(*idum);
for (j=NTAB+7;j>=0;j--) { /*Load the shue table */
/* (after 8 warm-ups).*/
k=(*idum)/IQ1;
*idum=IA1*(idum-k*IQ1)-k*IR1;
if (*idum < 0) *idum += IM1;
if (j < NTAB) iv[j] = *idum;
}
iy=iv[0];
}
k=(*idum)/IQ1; /*Start here when not initializing*/
*idum=IA1*(idum-k*IQ1)-k*IR1; /*Compute idum=(IA1*idum) % IM1 */
/*without overflows by Schrage's method.*/

if (*idum < 0) *idum += IM1;
k=idum2/IQ2;
idum2=IA2*(idum2-k*IQ2)-k*IR2; /*Compute idum2=(IA2*idum)%IM2 likewise*/
if (idum2 < 0) idum2 += IM2;
j=iy/NDIV; /* Will be in the range 0..NTAB-1.*/
iy=iv[j]-idum2; /*Here idum is shued, idum and idum2 */
/*are combined to generate output.*/

iv[j] = *idum;
if (iy < 1) iy += IMM1;
if ((temp=AM*iy) > RNMX)
return RNMX; /* Because users don't expect */
/*endpoint values.*/

else return temp;
}

```

## A.2 An Alternative Algorithm

Here, a printout of the algorithm proposed in Sec. 2.4 is presented. It can be easily implemented in the program shown in Sec. A.1. In order to do so, only the loop in the *main* function which counts the MCS has to be changed. Instead of incrementing the MC time always by one, it should be increased by the MC step width  $ts$  being a “variable” (actually, pointer) of the *simulation* function.

Again, we want to focus on one hole (NH=1). In this algorithm, first, an interval is calculated depending on the nearest-neighbors of the hole: All transition probabilities (defined by the Metropolis rates, Eq. (2.1)), of the hole and its nearest-neighbors are added up giving the upper limit *sum* of the interval (here,  $\tau_s = LP = TP \equiv 1$ ). Out of this interval  $[0, sum]$ , we draw a random number  $p$ . Now, we split the interval in the four successive, separate intervals out of which it is initially formed. Then, the exchange of the hole and the particle takes place in the direction associated to the interval which the random number  $p$  includes. In order to maintain the same time scale as in Secs. 2.1 and A.1, the time step width  $ts$  is, here, given by  $4/sum$ .

Comparing the different algorithms in Sec. A.1 and Sec. A.2, we find that the latter is about a factor two faster. Besides the fact that each trial is successful, the latter algorithm needs to draw only one random number which is the most real time-consuming process.

```
float simulation(on,hx,hy,iseed,ts)
/*ts - timestep*/
short int on[LX][LY];
int hx[],hy[];
long *iseed;
float *ts;
{
    int i,rh,rd,nn;
    float c,p,ran2(long *iseed);
    float s1, s2,s, sum;
    double exp();

    s = 0.0;
    c = 0.0;
    for (i=0; i<NH; i++){
        if (NH==1) rh=0;
        else
            rh=(int) ( NH * ran2(iseed)); /*choose hole */
        if (on[hx[rh]][(hy[rh]+1)%LY] == 1) s1 = (LP * exp(-E));
        else s1=LP;
        if (on[hx[rh]][(LY+hy[rh]-1)%LY] == -1) s2 = (LP * exp(-E));
        else s2=LP;
```

```

sum = 2.0 * TP + s1 + s2;
p = sum * ran2(iseed);
if (p < TP){
    if (on[(LX+hx[rh]-1)%LX][hy[rh]]==0) continue;
    else {
        on[hx[rh]][hy[rh]]=on[(LX+hx[rh]-1)%LX][hy[rh]];
        hx[rh]=(LX+hx[rh]-1)%LX;
        on[hx[rh]][hy[rh]]=0;
    }
}
if ((p >= TP) && (p < 2.0*TP)){
    if (on[(hx[rh]+1)%LX][hy[rh]]==0) continue;
    else {
        on[hx[rh]][hy[rh]]=on[(hx[rh]+1)%LX][hy[rh]];
        hx[rh]=(hx[rh]+1)%LX;
        on[hx[rh]][hy[rh]]=0;
    }
}
if ((p >= 2.0*TP) && (p < 2.0*TP + s1)) {
    if (on[hx[rh]][(hy[rh]+1)%LY]==0) continue;
    else{
        on[hx[rh]][hy[rh]]=on[hx[rh]][(hy[rh]+1)%LY];
        hy[rh]=(hy[rh]+1)%LY;
        on[hx[rh]][hy[rh]]=0;
    }
}
if (p >= 2.0*TP + s1){
    if (on[hx[rh]][(LY+hy[rh]-1)%LY]==0) continue;
    else{
        on[hx[rh]][hy[rh]]=on[hx[rh]][(LY+hy[rh]-1)%LY];
        hy[rh]=(LY+hy[rh]-1)%LY;
        on[hx[rh]][hy[rh]]=0;
    }
}
s += sum;
}
s /= NH;
*ts = (2.0*TP + 2.0*LP) / s;
}

```

# Vita

**Name:** Michael Thies  
**Date/Place of Birth:** November 13, 1971; Dissen aTW, Germany

**Education:**

1991–1993	Mechanical Engineering, Technische Universität Braunschweig, Germany
1993–1998	Physics, Technische Universität Braunschweig, Germany
1996–1997	Physics, VPI&SU, Virginia, USA (Exchange Stipend)
1998	Master of Science in Physics, VPI&SU, Virginia, USA